Fire and Heat Transfer Modelling of Small and Large Scale Experiments

by

Samaneh Zareian

A thesis
presented to the University of Waterloo
in fulfillment of the
thesis requirement for the degree of
Master of Applied Science
in
Mechanical and Mechatronics Engineering

Waterloo, Ontario, Canada, 2020

Author's Declaration

I hereby declare that I am the sole author of this thesis. This is a true copy of the thesis, including any required final revisions, as accepted by my examiners.

I understand that my thesis may be made electronically available to the public.

Abstract

The present work aims to provide insight on the small- and full-scale models of building construction materials and structures in fire scenarios. Steps are taken toward a long-term goal, which is to develop a complete model for heat and mass transfer across walls and in compartments in case of fire. This is an important aspect of fire safety engineering in which, with the help of in-depth knowledge of the fire on the buildings and construction materials and numerical methods, a complete understanding of fire behaviour can be obtained. Therefore, applications can be used to design safe buildings, analyze fire risks, and develop optimized egress models.

Experimental studies selected for the modelling are conducted at the University of Waterloo Fire Research Lab (UWFRL) for the validation and comparison of the simulation results. OpenFOAM, an open-source C++ toolbox for computational fluid dynamics modelling, is selected for modelling. In the first step, a small-scale heat transfer model presents the thermal prediction of construction materials at high temperatures in cone calorimeter tests. The model predicts the temperature well for two specimens exposed to constant and transient heat flux values. Improvements can be made using accurate thermophysical properties and a thermal contact model between layers of different materials. In the next step, a large-scale fire model is applied to an insulated compartment that is separated from another room by a steel wall, using Firefoam. Besides heat transfer, combustion, chemistry, and turbulence are included in the model. Large Eddy Simulation (LES) for turbulence, Finite Volume Discrete Ordinates Method (fvDOM) model for radiation and Eddy Dissipation Concept (EDC) for chemistry are employed. The model predicts the early stage of fire growth, but underpredicts the temperature during the decay phase. This tool can be used for future work as a first step toward a more sophisticated model for degrading and non-degrading wall assemblies in compartment fires.

Acknowledgements

I would like to express my sincere appreciation to my supervisor Professor Cecile Devaud for her continuous and valuable guidance, patience, and support throughout my Master's studies at the University of Waterloo. I am truly honoured to work with her in my research and learn from her helpful comments. I would like to take this opportunity to thank my committee members, Professor Elizabeth Weckman and Professor Patricia Nieva. Also, I would like to thank Professor Weckman for the advice and help with the questions related to the experimental work and fire dynamics. I would like to thank my friends and my research group team, especially Alex, for the constructive discussion in the office and support.

I would like to acknowledge the financial support from the Natural Sciences and Engineering Research Council of Canada (NSERC) and ROCKWOOL® company for this research. A part of computations were performed on the GPC supercomputer at the SciNet HPC Consortium funded by the Canada Foundation for Innovation under the auspices of Compute Canada; the Government of Ontario; Ontario Research Fund - Research Excellence; and the University of Toronto.

I cannot end without thanking my parents and my brother for their constant encouragement, support, and love, on which I have relied throughout the period of this work.

Dedication

To my loving family

Table of Contents

List of Figures

List of Tables

Chapter 1

Introduction

1.1 Overview

Discovery of fire is admittedly a turning point in human history. Its impact on everyday life and economy can be equally noticed as the significance of the invention of the wheel. While the first applications of fire may have been simple, the applications have evolved with our civilization. A glance at our local environment can illustrate the importance of fire. From heating our rooms or homes to daily transportation, fire plays a notable role. Outside of domestic applications, industrial processes rely almost entirely on fire and combustion. Many employ furnaces, heaters, ovens, and melters which work with combustion [1]. Fire is also used to terminate the products life cycles by waste disposal. Considering the importance of fire in our society, it is highly-valued to harness it precisely to get the maximum possible benefits.

Fire may be expressed as a manifestation of an exothermic chemical reaction [2]. It involves oxidation of a fuel resulting in the generation of reaction products and the release of thermal energy [3]. This generic definition can be applied to a simplistic candle flame or a huge, fully involved forest fire. Fire behavior is dynamic and depends on physical state and distribution of the fuel, the environment, and its nature over time. Mastering the complexity of fire behavior needs fitting engineering background in heat transfer, fluid

mechanics, and chemistry.

One of the earliest well-known examples of uncontrolled fire is the Great Fire of London, occurring in the 17th century. The fire destroyed 75% of the medieval city [4]. During the First and Second Great Fires of Toronto in 1849 and 1904, two people died, a vast section of the commercial core and many city blocks were demolished, and thousands of people were put out of work [5, 6]. These incidents confirm that there is always more need for consideration of inevitable fires and the feasible devastating impacts.

A very recent forest fire is the Gospers Mountain bushfire that happened in 2019. The largest wildfire in Australia lasted for several months, destroyed the nature and many buildings, killed many people and animals, and caused some endangered species to go extinct [7]. Another recent severe structure fire was Notre-Dame de Paris fire in 2019. As a UNESCO World Heritage Site, the cathedral is a precious site to human history, and and as a result of this devastating incident, many irreplaceable treasures and artworks were destroyed as well as the most parts of the wooden structure [8].

These are just a few instances of devastating uncontrolled fires that cause many life and property losses. Fire safety engineering can assist in preventing fires and in controlling the damages in the case of interest. Fire protection serves four goals of providing life safety, protecting property and heritage, continuity of operations, and narrowing the destructive environmental impact of fire. Fire safety views many aspects, from fire prevention to confining the propagation of fire and smoke, extinguishing a fire and the possibility of a quick response and the chance of safe exit. An uncontrolled fire can cause fatal damages; therefore, fire safety engineering plays a significant role in designing buildings. Unwanted fires can naturally occur or be caused by human activities.

One aspect of fire safety engineering is having an in-depth knowledge of the impacts of the fire on buildings and construction materials. In order to precisely predict the consequences of the fire and smoke in these cases, experimental and numerical methods can be utilized. Although the experimental studies are expensive financially and environmentally, they provide a thorough understanding of the fire behavior and also contribute as the databases to validate and evolve different fire safety software. Many standardized small- and large-scale fire tests are available in the literature [9, 10, 11, 12]. While small-scale

cases are cost-friendly and easier to set-up, in some cases, large-scale tests are required [13].

Nowadays, with the significant potential and enhancements in computational power and mathematical modelling, computational fluid dynamics (CFD) and fire modelling have become more widespread as research tools to guide us to a fuller knowledge of fire behavior. Although there are some simplifications necessary to make the computations feasible, CFD is a great approach to predict and model fire scenarios [14]. This approach can be applied to many different cases, from modelling small-scale cases to multi-compartment fire scenarios and complex geometries. Therefore, the predictions will be more precise, and applications can be used to design safe buildings, develop optimized egress models, and to analyze fire risks.

1.2 Objective

The goal of the present work is to assess heat transfer and fire models for set of small- and large-scale fire situations that relate to prediction of the thermal performance of construction materials under exposure to fire and smoke. Steps are taken for a long-term objective which is to develop a sophisticated model for heat and mass transfer. This is a engineering tool that helps the industrial research and development (R&D) community and engineers to design new building materials and assess products, so that they can assist in preventing fire spread among buildings, resulting in more control and less life and property losses.

A multi-phase modelling approach is implemented in combination with the heat transfer methodology using OpenFOAM (Open Source Field Operation and Manipulation), which is a C++ toolbox for developing customized solvers and utilities [15]. Firefoam [16] is used as the principal solver for developing the simulations the large fire test to predict the temperature which are compared to experimental data [10].

1.3 Outline

The presented work consists of four chapters. Chapter 2 provides an overview on relevant background information. Chapters 3 and 4 describe the assessment of a heat transfer model to predict behaviour of construction materials at elevated temperatures on a small-scale. Chapter 5 describes modelling a compartment fire. OpenFOAM is used for the numerical simulations and the results are compared to experimental tests that are conducted at the University of Waterloo Fire Research Lab. Finally, conclusions and recommendations are presented for future studies. The structure of the presented thesis and details are described as follows.

Chapter 2 covers relevant background information. Physical concepts in heat transfer and fire scenarios, the definition of fire, principle phenomena occurring in real compartment fire cases, small- and large-scale experimental methods, modelling methods, modelling steps, and their importance are discussed.

Chapter 3 presents a three-dimensional heat transfer model to predict the behaviour of construction materials on a small-scale. The focus in this chapter is modelling the performance of a two-layer specimen of insulation and concrete board exposed to constant incident heat flux, using OpenFOAM. The experimental study selected for the modelling helps to take the first step toward developing an engineering tool for the behaviour of small-scale building materials in detail at elevated temperatures. Additionally, in comparison to experimental methods, it is a time-efficient and environmentally friendly tool capable of investigating different scenarios. One of the main goals of the aforementioned experimental study is to measure and model the thermophysical properties of ROCKWOOL ® Safe insulation accurately, making the test case reliable for the thermal model development.

Chapter 4 assesses the capabilities and validation of the heat transfer model to predict the performance of a three-layer specimen on a small-scale. The specimen consisted of a steel plate, insulation, and cement board placed in a cone calorimeter. The specimen is exposed to transient heat flux during the experiment. The development of the CFD model is a starting point in modelling large-scale fire cases.

Chapter 5 presents a large-scale fire modelling. The modelled case consists of two com-

partments that are separated by a steel wall. A softwood pallet is burned at the centre of a compartment. FireFOAM is used for simulations. Different sub-models for combustion, radiation, and turbulence are used to get the most accurate results. Temperature measurements at various heights in the fire room and at the steel wall are compared with predicted results.

Chapter 6 provides the main findings, conclusions, and recommendations for future studies.

Chapter 2

Background

This chapter presents the physical phenomena happening in buildings in large and small scale in fire scenarios, from thermal degradation in wall assemblies to compartment fire stages. The state of available predictive models and the most applicable fire solvers are discussed. The heat transfer modes, the fire building code, fire tests, and fire solvers are discussed.

2.1 Fire Dynamics

Fire is a complex phenomenon and is an interaction between mass and heat transfer, fluid dynamics, material properties, combustion kinetics, chemistry, and structural mechanics. In this section, the key expressions and physical phenomena relevant to a fire scenario are described.

2.1.1 Combustion

In simple words, combustion is a chemical reaction of fuel and oxygen above a critical temperature. Fire triangle is referred to three components of fuel, oxygen, and ignition

source. Rapid oxidation needs an ignition source to initiate, which can be mechanical, thermal, chemical, or electrical. As the reaction proceeds, some gaseous products, heat, and light are generated due to the energy released by breaking chemical bonds.

Based on available fuel and oxidizer (among other factors), the combustion can be complete or incomplete. Complete combustion is preferred as the amount of products, which are water vapor (H_2O) and carbon dioxide (CO_2), are predictable. In incomplete combustion, in addition to water vapor and carbon dioxide, other products like carbon monoxide (CO), hydroxide (OH), the sulfur oxides (SO_2 and SO_3), oxides of nitrogen (NO_x) as well as carbon particles (soot) and ash may be observed [1].

2.1.2 Pyrolysis

At elevated temperature a thermochemical conversion with breaking down of liquid or solid fuel breaks down and realising volatiles occurs, called pyrolysis. The gaseous products form a combustible region near the original fuel, which can easily burn in case of having the three agents of the fire triangle [2]. One of the most prevalent materials in the study of pyrolysis is wood. With respect to fire safety concerns, wood is the superior construction material in houses, residential buildings, and furniture, which in case of compartment fires, undergo pyrolysis and combustion [17]. Understanding its behavior is a complex task in fire safety engineering. The pyrolysis of wood involves a multitude of constituents, such as cellulose, hemicellulose, lignin, and ash. Thermophysical properties and degradation vary in these components and they do not behave the same at elevated temperatures. The process of wood pyrolysis occurs within the range of 200°C to 500°C resulting in generation of char, tar, and volatile gases [18]. Therefore, an in-depth knowledge of mass transfer, heat transfer, and decomposition reactions is required to develop accurate prediction models for the complex phenomenon of wood pyrolysis [19].

2.1.3 Heat Transfer

Thermal energy is an internal property of material related to the temperature of the object. Heat is thermal energy in motion from a hot region to a cold one. There are three heat transfer modes, known as conduction, convection, and radiation [20].

Conduction occurs when there is a temperature gradient between two points in a medium. Conduction exists for all kinds of material states and is quantified by Fourier's law. However, it is the most important form of heat transfer in solids and at the contact of fluid and solid. For a one-dimensional conduction, Fourier's law can be written as:

$$q_{cond} = -kA\frac{dT}{dx} \tag{2.1}$$

where k is the thermal conductivity (W/mK), A is the cross sectional area at which the heat is transferred (m^2), $\frac{dT}{dx}$ shows the temperature gradient in the x direction (K/m), and q_{cond} is the rate of conductive heat (W) [20].

Convection is the mechanism induced by movement of a liquid or gas exposed to thermal gradient. It is calculated using the following equation:

$$q_{conv} = h_c(T_g - T_s)A, \tag{2.2}$$

where h_c is the convective heat transfer coefficient between the solid and the adjacent fluid (W/m^2K), T_g and T_s are the respective temperature of the two points in fluid and nearby solid (K), A is the solid surface area that is in contact with the fluid (m^2), and q_{conv} is the rate of convection heat transfer (W) [20].

One of the challenges in convective mode is to determine the convective heat transfer coefficient (h), which depends on the solid and fluid materials, temperature, flow regime and geometry. Based on these factors, empirical expressions can be used which relate the convective heat transfer coefficient to Reynolds number (Re), Prandtl number (Pr), Rayleigh number (Ra), and Nusselt number (Nu). The Reynolds number (Re) represents the domination of inertia forces to viscous forces. It also specifies the regime of the flow whether it is laminar, transient, or turbulent. The Prandtl number (Pr) describes the ratio

of the momentum diffusivity to the thermal diffusivity. The Rayleigh number (Re) also describes the flow regime and natural convection. It is the product of the Prandtl number (Pr) and the Grashof number (Gr) which represents the relation between buoyancy and viscosity. The Nusselt number (Nu) describes the ratio of convection to pure conduction. This is the key parameter which connects the experimental expressions to the convective heat transfer coefficient. In some cases, it is preferred to use an experimentally determined value of the convective heat transfer coefficient for a similar experimental setup.

Radiation is the heat transfer mechanism through which heat is transmitted by electromagnetic waves, meaning that it requires no medium. It can be quantified using the following equation:

$$q_{rad} = \varepsilon\sigma({T_2}^4 - {T_1}^4)A, \tag{2.3}$$

where ε is the emissivity of the surface, σ is the Stephan-Boltzmann constant ($5.6704 \times 10^{-8} W/m^2K^4$), T_2 and T_1 are the respective temperature of the emitting and absorbing surfaces (K), A is the emitting surface area (m^2), and q_{rad} is the rate of radiative heat transfer (W) [20].

When a fire initiates in an enclosure, heat transfer affects the entire domain. Therefore, a complete understanding of heat transfer is required to analyze and build fire models. Convection and radiation are the significant modes in the fire plume itself. In the early stages for medium to large fire sizes, convection is the dominant mode. As the fire evolves and the temperature increases, radiation becomes more significant. Hot ceiling, flames, hot gaseous products, and particles contribute to radiation. Thus, convection occurs in the room and at the interfaces with the walls while the air is circulating, and radiation transfers heat to any object in the room, which may lead them to ignite too. There is also conduction occurring at the wall assemblies due to the thermal gradient. When a fire happens in a room, the heat transfer to the nearby rooms can increase the rate of damage and the fire spread. Therefore, a study on conduction in wall constructions is critical. Heat transfer in wall assemblies is a complex phenomenon, and factors such as different layers of materials, their configurations, and time exposed to heat source are some other challenges in this topic [21].

2.1.4 Heat Release Rate

Heat release rate (HRR) is the most commonly used parameter to characterize a fire. It quantifies fire size, risk, and its intensity [22]. It is the amount of energy generated by fire per unit time and can be expressed as:

$$\dot{Q} = \chi \dot{m}_f{}'' A_f \Delta H_c. \tag{2.4}$$

In Eq. 2.4, A_f is the fuel surface area (m^2), $\dot{m}_f{}''$ is the mass fuel burning rate ($g/m^2 s$), ΔH_c is the heat of combustion of the fuel (kJ/g), and χ is a positive factor to consider incomplete combustion [2]. HRR depends on not only the material of the fuel itself (e.g., chemistry and physical form) but also on the environmental conditions (e.g., ventilation and the location of the fire). Many factors contribute to the determination of HRR; therefore, small- and room-scale experimental tests can be used to get the HRR values for different fuels. Many empirical correlations are derived to determine $\dot{Q}$. Based on the material, the peak of fire HRR curves can be categorized into different ranges. Moreover, HRR values are used to classify the fire growth rate to slow, medium, fast, and ultra-fast, which relates to various materials. It is also used to determine the detector response time and quantify hazard risks. Greater values of HRR often result in more smoke production, radiation, and toxic products of combustion.

2.1.5 Turbulence

Fluid flows may be classified into two groups: laminar and turbulent flows. This classification is conducted using the Reynolds number for the specific geometry of the case. At higher Reynolds numbers, where the inertial forces are more significant than viscous forces, fluid flow is turbulent. A turbulent regime is random in nature, three dimensional, and time and space variant. One main characteristic of turbulent flow is the ability to cause effective mixing in the fluid. This is extremely valuable in industrial and engineering applications. In engines and reactors, turbulence is beneficial as the fluid must mix thor-

oughly to raise the efficiency of combustion [23]. However, turbulence in fires increases the burning rates and accelerates the fire spread, therefore, intensifies the destructive impact.

2.1.6 Turbulence Modelling

There are three approaches to model turbulent flows: Direct Numerical Simulation (DNS), Reynolds Average Navier-Stokes (RANS), and Large Eddy Simulation (LES).

DNS solves the Navier-Stokes equations directly, which requires enormous computational power. It is generally applicable for low Reynolds numbers and simple geometries, resulting in the most accurate predictions [24].

In RANS, continuity and Navier-Stokes equations are revised based on the statistic concept that while quantities are random, they can be characterized by their probability density functions (PDF). Any turbulent property consists of two components, statistically: the mean value and the fluctuations. Consequently, additional unknown terms for velocity fluctuation components, also known as Reynolds stress tensor, are generated in the momentum equation. Then, to overcome the closure problem, some simplifying assumptions such as having two-dimensional statistical flow and irrotational motion are needed resulting in less unknown velocity fluctuation terms. For particular types of flows like free shear flows, Reynolds stresses reduce to six nonzero terms. Then, a two-equation model is typically selected based on the flow regime. Turbulent viscosity relates two parameters expressed in the two aforementioned equations. Using the Boussinesq assumption, the Reynolds stress tensor is related to the turbulent viscosity and can be determined [23]. In comparison to DNS, RANS is faster and may provide first approximations. The main disadvantage of this approach is that it is not suitable for all types of flows due to simplifications and assumptions made to derive equations.

The proposal and development of LES initiated in 1963 by Smagorinsky, a meteorologist who was working on atmospheric boundary layers [25]. In LES, each quantity is decomposed into two terms employing spatial filtering operation: the filtered or resolved component and the residual or sub-grid component. The Navier-Stokes equations are in

standard form with additional terms for residual or subgrid-scale (SGS) stresses. The equations are solved for large energy-containing eddies, while small-scale eddies are modeled. The ideal filtering width is the size of small-scale eddies in the inertia sub-range. Moreover, the grid spacing should be as large as large-scale turbulence motions are [23]. Generally, an eddy-viscosity model for SGS tensor is used to overcome the closure problem.

The LES approach lies between the RANS and DNS methods with respect to the accuracy and computational power needed. In DNS, all the scales are directly solved, resulting in a massive computational cost. Large scale motions which are responsible for the considerable portion of momentum and energy transfer are directly solved in LES, while they are modeled in RANS. Additionally, since the SGS components are more homogeneous and isotropic, they are simpler to model than unclosed terms in RANS. Although there are some challenges and ongoing research on complex chemical reactions that occur at the small scales, for turbulent combustion, even a simple SGS model has the potential to provide better predictions than RANS results [24]. Thus, LES is a proper approach for transient, turbulent combustion that happens in fire and is selected for the fire modelling in the current work. More discussion is provided in Section 5.2.2 on turbulence modelling for the fire simulation.

2.1.7 Compartment Fires

One of the principal aspects of fire safety engineering is the study of compartment fires due to the complexity and vast application [26]. By advancing understanding compartment fires, the structure design can be improved, and the damages can be reduced.

The present work is mostly directed toward compartment fires, meaning fires confined in an enclosed space that has a constant volume. This can occur in residential buildings, transportation like vehicle fires, airplanes and trains, and industry.

Some of the characteristics of compartment fires are listed here [26]:

- Gaseous combustion products gather below the ceiling in the confined space due to buoyancy.

- The source of oxygen is limited. Thus, after some time, deficiency in oxidizer causes flame extinction. This may occur in different stages.
- Unburned fuel may be left in case of having an under-ventilated fire.
- Soot may be generated in cases of slow mixing times.
- The hot and cold layers are completely recognizable. The hot layer accumulates at the top room near the ceiling, while the cold gas remains at the bottom. The temperature and density difference cause hot and cold layer stratification.
- In compartment fires, the fuel source is often unconventional. In compartment fires, most objects are combustible such as chairs, sofas, beds, cloths. Any nearby object to fire serves as fuel and accelerate the fire spread. The great amount of available fuel is one of the facts that make these fires dangerous.
- Physical obstructions, like walls, partitions, and furniture, can significantly affect the fire spread and the mechanisms.
- Compared to jet flames or any internal combustion engine, the velocity scales in compartment fires are about 0.1 cm/s to 10 cm/s, which is relatively small.
- One important phenomenon which may occur in compartment fires is flashover. Flashover is the drastic magnification in fire conditions. Situations that can cause flashover are:
  - Exposure of fuel-rich gases to oxygen (air), which results in a phenomenon called backdraft.
  - Sudden fire spread in the compartment due to the increase in the burning rate of the unconventional fuel
  - Fast ignition and fire spread as a result of an increase in heat flux

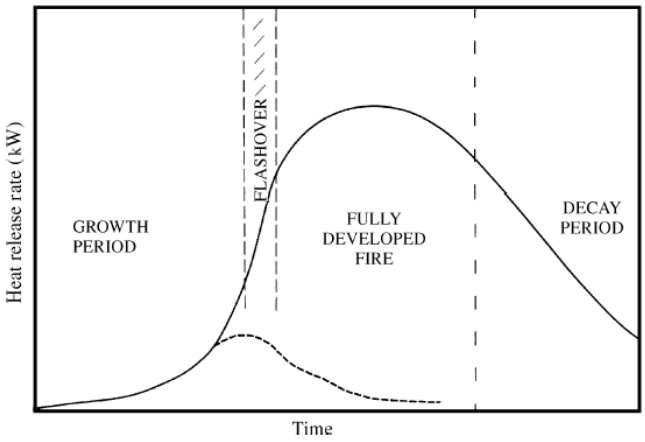

Figure 2.1: Stages of compartment fire development for a well-ventilated case. The dashed line shows the cases of insufficient oxygen or fuel before flashover. Reproduced from [2]

Stages of Compartment Fire Development

Figure 2.1 shows the stages of the development of compartment fires. Each stage is described as follows [26, 21].

Ignition With the presence of the fire triangle, fuel, oxygen, and activation energy, the combustion can begin. In a compartment, the oxygen usually exists as a constituent in air at the beginning. The fuel can be a hydrocarbon pool or a part of furniture. There are two ways for ignition to commence: piloted and non-piloted. In piloted ignition, an external high-energy source, such as a flame, electrical, or glowing wire, or a spark comes in contact with gaseous combustible material. Non-piloted (or spontaneous) ignition occurs by raising the flammable material temperature above its auto-ignition temperature without having any other external source.

Growth Following ignition, the fire starts growing. In this stage of development, the oxygen concentration is almost constant, and the average temperature of the compartment is relatively low. There are some local high temperatures at the edges of the fire plume and under the ceiling. The fire burns at its origin as if it is in the open air, and it is not influenced by the geometry of the compartment or the boundaries.

Flashover While the fire is developing, the flames spread to nearby objects, and the fire grows in size. At this stage, the interaction between fire and compartment boundaries increases. As a result, rapid propagation of fire and its significant incident radiation make every combustible surface involved in fire. This relatively quick transition is called flashover.

Two common terms in compartment fires are ventilation-limited and fuel-limited fires. Fuel-limited fire occurs when excessive amount of oxygen exists, and fire development relies on the availability of fuel source. In ventilation-limited case, the oxygen concentration in the smoke layer is almost zero. Moreover, there are significant amounts of smoke, CO, and released energy. Flashover is marked as the point before which the fuel materials mostly dominate the fire and now is mostly influenced by the ventilation conditions and compartment geometry. It is a crucial physical event in fire scenarios. The safest time to escape a compartment fire is before the time flashover happens.

Flashover occurrence is regulated by many factors, like the compartment geometry, the arrangement of ignitable objects, the nature of the fuel, and the availability of oxygen and fuel.

Fully Developed After flashover, the fire is in a fully developed or post-flashover stage in which all the combustible materials are entirely involved in fire to the maximum potential and flames fully encompass the entire space.

Based on the amount of air supply available, this stage can be ventilation-limited or not. While compartment fires are mostly ventilation-limited at this phase, the fully-developed fire can be strong enough to break the windows to provide oxygen from fresh air. In this situation, the fire is no longer ventilation-limited and would not be extinguished until the entire fuel supply is burned.

This phase is seriously threatening for any occupant in the room or the building and causes dramatic damages. The temperature can easily reach 1100 °C and toxic gaseous combustion products, dark smoke, and a high amount of soot are present. The elevated temperature may cause the structural load carrying members to fail. As a result, the building may collapse and put nearby structures at risk.

Decay At any stage, when one of the components of the fire triangle is no longer available, fire can extinguish. Decay is marked as a stage at which the average temperature drops to 80 % of its peak value. At this phase, the fire burns slowly and the total heat release rate drops significantly.

2.1.8 Construction Materials and Models

From the fire safety engineering point of view, wall assemblies are the chief components to stop or mitigate fire spread from one room to another. In addition to necessary knowledge on heat transfer mechanisms, which were discussed earlier, an in-depth understanding of construction materials behavior at elevated temperatures can pave the way to develop predictive models for large-scale fire cases. Two regions of study can be noted. First, the temperature-dependent properties of materials must be investigated. Second, the complex process of thermal degradation and deformation of the materials must be understood. Then, it is feasible to develop an accurate model based on detailed knowledge. In general, wall assemblies consist of metal or wood studs, insulation, and gypsum boards.

Wall Studs Typically, steel skeletons are used in multi-storey and large buildings, and wood studs are commonly used in frames in both small and large buildings [17, 27]. Although the steel frames do not degrade at elevated temperatures, they expand thermally, deform, and when they reach their yield strength, they are not capable of bearing the structural load. This concern is very likely to happen in fire scenarios since the critical temperature of the lightweight steel frames (LSF) is approximately 350-400 °C [28]. Wood is more complicated in the fire as it is a non-homogeneous and non-isotropic material consisting of cellulose, hemicellulose, lignin, and ash. At a temperature of 100°C, the water starts to be vaporized, which demands a large amount of input energy. At temperatures higher than 200°C, the constituents decompose and generate char [2]. In a wall exposed to high temperature, the char layer starts to develop on the side of the wood stud in contact with the high-temperature side of the gypsum board and continues to develop on the sides in contact with the air cavity [29, 30]. From 200°C to 500°C, pyrolysis occurs, which generates char, tar, and gases like carbon dioxide and methyl alcohol [31, 18]. Some

challenges in this area are moisture movement, shrinkage of the wood studs, and modelling radiation through the char, as well as the exact chemical reactions taking place [32].

Insulation The main goal of installing insulation is to block sound and heat transfer to bring human comfort. Nowadays, the new application of insulation materials is to mitigate fire spread. Two commonly used groups of inorganic fibrous insulation (glass wool and stone wool) and organic foamy insulation (expanded and extruded polystyrene and polyurethane foam) exist in the market. Glass wool and stone wool have the same basic materials and are the popular insulation types. Stone wool is designed to have a high melting temperature be more suitable for fire resistance [33].

Gypsum Gypsum boards act not only as the covering layers of the wall structures but also as the fire resistance layers. Each board consists of a noncombustible core and papers on the top. The core is mostly $CaSO_4.2H_2O$. 21% by mass of the core is chemically bound water, and there is a small amount of absorbed water. For temperatures above $80 - 100°C$, after dehydration at a slightly lower temperature, calcination begins. The heat transfer through the gypsum board is significantly decelerated due to the fact that the available amount of water in the gypsum board consumes a large amount of released energy (625 kJ per 1 kg of gypsum) [30]. The heat has a delay in moving across the board until the calcination is completely done. At temperatures between $100 - 160°C$, 17.5% of the mass of the gypsum board is lost by the water driven off. One complex phenomenon occurring at elevated temperature is the shrinkage. The gypsum board starts to lose its flexibility and strength at around 400°C and 500°C, respectively. Therefore, starting from 400°C, the gypsum sheets gradually open and pull off the screw at high temperature of approximately 700°C [34]. When the joints open, the hot gas enters the space between the sheets, causing the inner paper layer to burn off and causing the wood to generate char quickly. Moreover, the papers covering the core slough, which reduces the thickness of the board [32].

There are two kinds of gypsum boards with standard thicknesses: Type X (15.9mm) and Type C (12.7mm). The Type X gypsum plasterboard includes materials to mitigate fire spread better like fiberglass; therefore, it is usually referred to as the fire-resistant gypsum plasterboard [35]. Detailed studies on gypsum behavior are provided by Lazara et. al. [35] and Yu and Brouwers [36]. Although there are numerous studies on gypsum board

properties at elevated temperatures, there are still uncertainties in this area of research demanding more investigation [37].

As discussed, different mass loss rates and chemical reactions take place at various temperature ranges for the non-homogeneous materials of wall assemblies. Additionally, the determination of thermophysical properties of each phase of the material, the porosity, moisture movement, the emissivity, and the enthalpies bring notable complexity to coupled momentum, heat, and mass transport equations. Small-scale tests can provide valuable information on the behavior of construction materials and their exact thermophysical properties in fire scenarios. This information can be input for large-scale models. Wall2DN [34], CUWoodFrame [38], and ADIDRAS [32] are some of these models. Fire resistance of the wall construction is measured using standardized tests, which are illustrated in the next section.

2.2 Fire Building Codes

Fire safety can be evaluated using two approaches: a prescriptive-based or a performance-based approach [39, 40]. The traditional prescriptive-based approach is rooted in the 19th century. It describes regulations for building designs, structure, and maintenance. Although the strategy is suitable for regular buildings, it cannot provide sufficient safety protection for complex buildings, such as structures with high ceilings, large houses, or power generation facilities in which a small fire is a considerable risk [41].

For over two decades, engineered performance-based fire protection approaches have been preferred in codes and guidelines worldwide. There have been challenges remaining a potential to improve [42]. Unlike the prescriptive method, the fundamental concept of a performance-based approach is not to prescribe solutions but rather to demonstrate that the design meets defined objectives. The objectives are translated into quantifiable parameters as the tools to estimate the performance of a proposed design to validate compliance with the required performance parameters [40]. As a result, there is a potential for innovation and novel developments. Moreover, designs can be cost-effective, and international trade may be enhanced.

In Canada, the National Building Code of Canada (NBC) provides the regulations for fire protection. It is usually updated every five years through a consensus process and published by the National Research Council of Canada (NRC) [43]. In the desired structure, the assemblies (e.g., wall, floor, roof, column) act as fire separations, so the proper fire separation limits the fire spread. Fire resistance rating, which is a parameter to determine the level of fire protection of separations, is measured using different standardized tests. This characteristic time is the duration for which the wall specimen exposed to a specific controlled heat or fire exposure does not undergo thermal or structural failure as defined by the test. In Canada, fire resistance rating is determined using prescriptive ASTM E119 [44] or CAN/ULC-S101 [45] tests.

2.3 Fire Test Methods

In general, fire tests can be categorized into two groups: small-scale and large-scale. Some of the small-scale tests are conducted in a cone calorimeter which determine the effect of elevated thermal exposure on a reduced scale of construction materials to evaluate fire safety criteria. Although these tests do not provide the behavior of the specimen in a real fire scenario, they are time-saving, cost-efficient, and safe. Large-scale tests investigate the fire growth and its impact on the realistic structure. Although these tests are expensive and risky, they provide a systematic understanding of the fire scenario. These tests are necessary to understand fire behavior and consequences. Therefore, the experimental data on temperature, chemistry, and heat flux can be used to develop empirical correlations and improve numerical models. This project mainly focuses on the behavior of construction material in elevated thermal exposure in small-scale and model the compartment fire tests on large-scale.

2.3.1 Cone Calorimeter Tests

One of the common small-scale test methods is the cone calorimeter test. The specimen is placed on the cell load and exposed to a constant or time-variable heat flux from the

conically-wound electric resistance coil. During the test, many quantities can be measured, such as mass loss rate (MLR), porosity, specific heat, conduction, heat release rate (HRR), and temperature. Moreover, time to sustained flaming and gas concentration can be measured. Pyrolysis, visible smoke development, and ignition of the test specimen can be noticed, and damages can be recorded.

ASTM E1354-17 provides a detailed description of the experimental apparatus and standard operation of the test method [46]. ASTM E967-08 [47] and ASTM E968-02 [48] are used for temperature and heat flow calibrations.

Figures 2.2 and 2.3 present the overall view and detailed view of the cone calorimeter [46]. All dimensions are in millimeters. A standard planar specimen can have a size of 100 mm×100 mm and a thickness of a maximum of 50 mm. The test specimen is wrapped in aluminum foil and is mounted on a layer of refractory fiber blanket on the load cell. The holder is made of 2.4 mm thick stainless steel with interior dimensions of 101.2 mm×101.2 mm, and 22.6 mm deep. The outer shell of the cone heater is constructed of stainless steel and inside there is an electric heater element made of tungsten. At the bottom of the heater, there exists a stainless steel radiation shield to protect the test specimen from any preheating before the starting of the test. To conduct the test, the cone is heated to a user-defined temperature and stay at the specified temperature for at least 10 minutes for stabilization. Finally, the shield is opened, and the test case is exposed to the radiation [46]. All the measurements can be conducted based on different standardized test methods and empirical correlations. For example, the heat release rate can be estimated based on changes in oxygen concentration at the exhaust and volumetric flow rate.

2.3.2 Full-scale Compartment Tests

Standard test methods prescribe outlines and quantified parameters to assess the fire performance of construction materials and assemblies. One of the most widely accepted test methods is ASTM E119, developed by the American Society of Testing and Methods and is one of the first adopted fire tests in 1918. It was developed as a result of a huge drastic fire in Baltimore in 1905. ASTM E119 measures the response of the material and assembly to

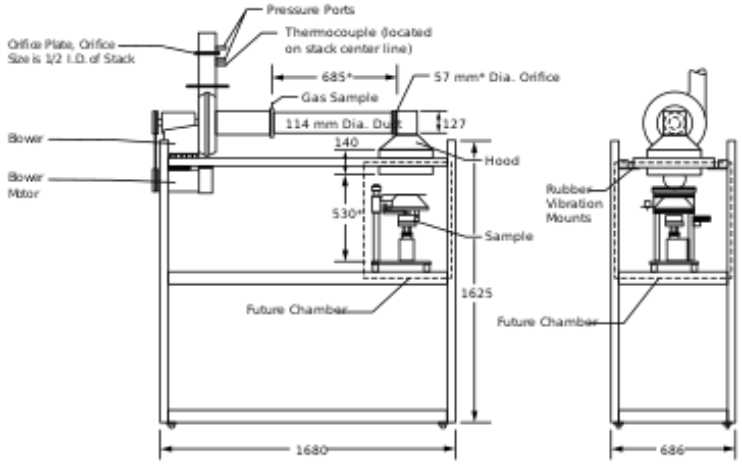

Figure 2.2: Overall view of cone calorimeter; Reproduced from [46]

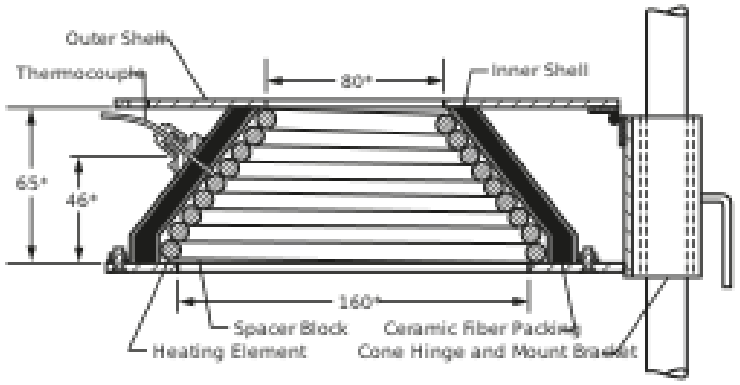

Figure 2.3: Schematic of cone heater; Reproduced from [46]

flame or heat under controlled conditions. In this test, a construction assembly is installed in a gas-fired furnace. The temperature of the furnace follows a temperature-time curve defined in the standard method, and the temperature is measured on the unexposed side. The failure occurs when one of the following situations happens first:

- The increase in the average temperature on the unexposed side is more than 140°C.
- At any location on the unexposed side, the increase in temperature is more than 180°C.
- Cotton waste on the unexposed side is ignited through the cracks generated during the test.

ASTM E603-17 provides a guideline for designing room fire experiments and interpreting the results [49]. It helps to plan to obtain fire-response properties of material and assemblies and output data for room fire tests to make fire safety regulations and improve fire models. This guideline helps to understand whether the small-scale tests adequately measure the fire hazard potentials and how the scaling parameters affect results. ASTM E2257 is one of the key standard test methods used to evaluate the performance of the wall assemblies, roof, floor, and all the coatings together in a fire scenario. In this test, the impact of fire growth on the structure with an open doorway as well as species measurements, time to flashover, and heat flux are measured [50]. With respect to fire safety engineering, a deep understanding of construction materials in fire along with modelling techniques will save lives, money, and the environment.

2.4 Fire Models

Mathematical fire modelling is an interdisciplinary field that can bring deep insight to fire investigators, fire protection engineers, forensics engineers, designers, and researchers. It provides valuable information on the interaction between fire and the environment. This information is beneficial in two ways. Firstly, it can enhance our understanding of the

flame spread. So, it is a relatively cost-efficient tool to reproduce and study real fire scenarios. Secondly, fire modelling can be used to analyze the performance of the design and distinguish the practical factors to reduce the risk. As a result, modification can be made to have safer designs for egress and optimized fire protection equipment. The models are developed using fundamental concepts of heat and mass transfer, thermodynamics, turbulence, and chemistry. In the 1940s, the study on the interaction on fire and environment started using available experimental data. Early development of models started in the 1980s, and rapid advancement being made during the 1990s [2]. To make the modelling feasible and efficient, various simplifying assumptions in equations have been employed. However, with the modern enhancement in computational power, real fire models can be more accurate and less simplified nowadays. The main challenging areas in fire modelling are degradation, pyrolysis, combustion, and flashover. The procedure of combustion depends on available fuel and oxygen, which leads to different sets of reactions. Also, the prediction of the generation of soot as a functioning component in thermal radiation should be taken into account. Flashover is a spontaneous event that happens very quickly in the field and leads the items to burn. A suitable model for flame spread can improve accuracy. A significant amount of research now focus on the behavior of materials at elevated temperatures. Mainly, in the case of pyrolysis and degradation, the behavior is complex and temperature-dependent. The mass transport, vaporization, and changes in the burning material and its volume add challenges to modelling.

Three main categories of fire models are algebraic models, zone models, and field models. Each can be divided into sub-models. These sub-models developed based on their specific application. They investigate different purposes of fire behavior and smoke movement, building evacuation (egress models), fire and sprinkler interaction, fire suppression, risk, and hazard [51]. Based on the study case, the researcher or the investigator must choose the most suitable model. Factors that contribute to decision-making include physics, implementation, numerical solvers, assumptions, limitations of the model, and cost.

The first step employed to study a fire scenario is applying algebraic models. These early models consist of two groups. Firstly, they can be empirical correlations developed based on fire experiments and similarity analyses. The second group is the physical expressions,

which can be directly calculated based on physical phenomena. The main goal of these models is to yield rough estimates and information about the fire scenarios immediately. This is useful for hands-on calculations and engineering designs. They can provide an approximate representation of fire behavior and variables like flame height, heat release rate, plume and ceiling jet velocities, gas layer temperatures, and sprinkler actuation time [2]. In addition, the expressions, used appropriately, can be advantageous benchmarks to check the values or the order of the magnitude of the results achieved by zone or field models.

The next step to provide more details is to use zone models. The original models were developed at Harvard University by Mitler, Rockett [52, 53] and Emmons [54] in the late 1970s and early 1980s. The first model developed to study a single compartment fire, and gradually, it evolved to consider multi-compartment fires and many correlations in fire scenarios. Typically, in a zone model, there are at least two or three control volumes, called zones. These zones can be the hot (upper), cold (lower), and fire plume regions and can be more detailed if desired. The properties in each zone are uniform, and mass, energy, momentum, and chemical species conservation equations are balanced. Besides, empirical correlations are often used particularly in sub-models, which are generated for specific purposes [55]. Although there are major simplifications in developing zone models [56] and they are not capable of modelling complex geometries, the low computational cost and relatively realistic results make these models a suitable option for ordinary cases. Since a few decades ago, many zone models have been introduced. Among them, CFAST developed by the National Institute of Standards and Technology (NIST) [57] and OZone developed in Liege University [58] are counted as the most popular ones.

The last modelling tool is the field model, also known as computational fluid dynamics (CFD) model. This approach presents a finer level of resolution by dividing the area of study to desired small control volumes. Using CFD techniques, the conservation equations for mass, energy, momentum, and species are solved for each cell over time, resulting in the history of the fire evolution. With the advances in computational power, this approach is capable of modelling sophisticated fire scenarios. In CFD models, complex phenomena such as combustion, pyrolysis, soot generation, turbulence, and different modes of heat

transfer can be accounted for using empirical or developed physical models. Field models are flexible, allowing a wide range of boundary conditions to complex geometries to be applied. However, this requires a detailed user guide for the expertise with the knowledge in the field to set up and run the simulations. On the other hand, it is critical to determine fire growth. To estimate fire growth or HRR, usually, the global burning rate based on the material is used. The constant HRR value over time is a notably simplified assumption. Moreover, evacuation and fire damages are some complex aspects that need more research to be accounted for in advanced models. CFD models are the most precise tools to predict sophisticated fire phenomena, such as flame spread, smoke movement in multi-compartment, and structure of the fire plume [2].

The present work is mainly focused on computational fluid dynamics using fire modelling in order to predict small and large scale fire experiments. Therefore, in the next section, CFD techniques and procedures are reviewed.

2.4.1 Field (CFD) Models

Computational fluid dynamics is an analytical technique to study the behavior of flow, and correlated mechanisms like heat transfer and chemical reactions [59]. CFD is a practical and flexible tool that can be applied to a wide range of simple to complex applications in research and industry, including aerodynamics, biomedical engineering, engine combustion, building designs, weather, and pollution analyses.

The numerical algorithm for any CFD model consists of the following main components: a pre-processor, a solver, post-processor.

In pre-processing, the first step is to creat the geometry of the case. Then, the domain is divided into small control volumes or cells. The properties in each cell are uniform. The case must be grid-independent, meaning that the grid or mesh must consist of sufficiently small cells so that the results would not change greatly upon changing the mesh refinement. Usually, solvers are compatible with other powerful design softwares. Therefore, the geometry and mesh generation can be conducted in any other suitable software and then imported to the main solver software. Next, the properties of the materials and physical

and chemical phenomena must be specified. Finally, the initial and boundary conditions must be determined. This stage of modelling is the most time-consuming part for the user [59]. The decisions on mesh refinement must be made cautiously in order to have sufficiently precise results in a reasonable timeframe.

The solver uses finite volume methods and considers the accuracy needed to discretize the differential equations. In this step, the iteration size is determined so that it justifies the convergence criterion.

For post-processing, graphical tools assist in data visualization. The post-processing step aims to facilitate the interpretation of the simulation results. This step results in displaying line or contour plots for quantities such as temperature, pressure, concentration, or velocity.

Unavoidable sources of uncertainty in developing a solver require the step of verification and validation. In a CFD-based solver code, a system discretized form of non-linear partial differential equations of conservation of mass, momentum, and energy are implemented. Based upon the case of the study, equations for chemical reaction or turbulence must be taken into account, too. Three main areas of the source of numerical errors include round-off error, iterative convergence error, and discretization error [59]. The verification and validation process is a cycle, with the starting point of developing the CFD-based code. The equations must be verified using other computational solvers to check if they are solved correctly. Next, the algorithm must be validated using available experimental data to check if the results agree with reality. Finally, if needed, the code is revised, and the steps are repeated [60]. In fire research, there is a specific urge for the validation step [61].

2.4.2 CFD-based Solvers

Nowadays, there are many powerful commercial CFD packages such as ANSYS Fluent [62], ANSYS CFX [63], and COMSOL Multiphysics [64]. With the focus on fire modelling, there are specialized CFD-based solvers, including ISIS [65] developed by the Institut de Radioprotection et de Sürete Nucleaire (IRSN), FDS developed by NIST [66], SIERRA/Fuego

developed by Sandia National Laboratories (SNL) [67], and FireFOAM built on the OpenFOAM platform [15, 16].

This study uses OpenFOAM (Open Source Field Operation and Manipulation), an open-source CFD package, for the modelling. OpenFOAM is an object-oriented software library written in C++. ChtMultiRegionFoam and FireFOAM are the solvers utilized in order to model heat transfer and fire cases. OpenFOAM is a powerful CFD package useful for research purposes as it can be modified with respect to the application and the case of study. Several studies are available in the literature that validate OpenFOAM, especially for fire scenarios [61, 68, 69]. In this study, the computational resources are provided by supercomputer cluster SciNet for running the cases in parallel. Overall, OpenFOAM was found to be a proper choice for research and modelling focused on fire experiments.

Chapter 3

Thermal CFD Model for Cone Calorimeter Tests

This chapter illustrates the assessment of a CFD model for analyzing heat transfer through a specimen under a cone calorimeter. The experimental study is selected from one of the studies at the University of Waterloo Fire Research Lab (UWFRL). The model has been implemented in OpenFOAM. The experimental setup, model formulation, computational domain, mesh, numerical schemes, boundary conditions, and properties are presented in this chapter. Finally, the results are compared with the experimental data and conclusions are made.

3.1 Experimental Details

The cone calorimeter test selected for the study is conducted by N. Nagy at the UWFRL [70]. A cylindrical specimen comprising a layer of insulation and a cement disc is placed under a cone calorimeter heater. The top layer is made of ROCKWOOL ® Safe insulation. ROCKWOOL ® Safe insulation is a dense type of mineral wool insulation conventional in residential, commercial, industrial, and marine applications. It contains 94-99% mineral fibre and 1-6% CUEPF binder. At an elevated temperature of 600 °C, the CUEPF binder

is subjected to a mass loss of nearly 80%. The insulation has a nominal density of 72 kg/m^3, with a thickness of 54 mm to 56 mm for different tests. Under this layer, a 7.7 mm thick cement board is placed. The diameter of the disc-shaped specimen is 230 mm, large enough to avoid any rollover of the test case. Two K-type thermocouples are placed on the top surface of the insulation at the radii of r=0 and r=70 mm. In addition, two other K-type thermocouples are affixed to the cement board located at the insulation and cement board interface at the same radial distances. Figure 3.1 shows the schematic of the test case under the cone calorimeter heater. The cylindrical specimen is mounted under the cone calorimeter heater on the load cell. There is a distance of 25 mm from the bottom of the heater to the specimen. The cone calorimeter heater has a height of 68 mm, and its top and bottom diameters are 80 mm and 160 mm, respectively. The test case is exposed to constant incident heat flux values of 25 kW/m^2 and 50 kW/m^2. Temperature quantities are measured and collected at the four thermocouple locations [70].

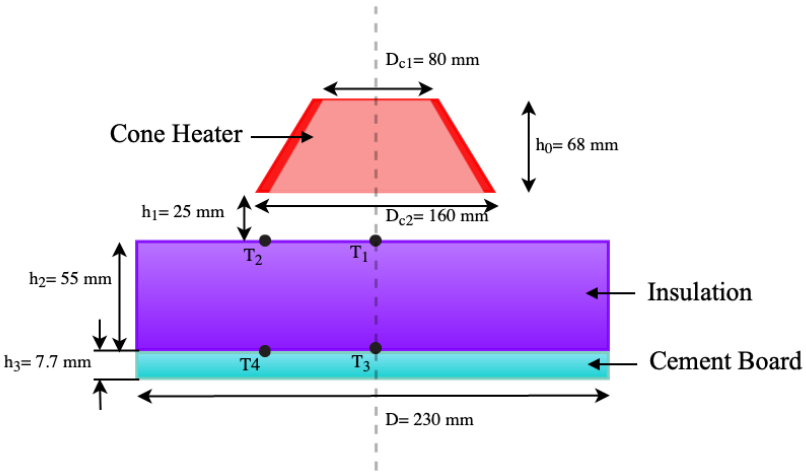

Figure 3.1: Schematic of the two-layer specimen under the cone calorimeter heater

3.2 Computational Details

In this section, the modelling approach is explained. OpenFOAM with the solver ChtMultiRegionFoam is selected as the base platform to solve the governing equations to predict thermal responses of the specimen in four experiments.

3.2.1 Governing Equations

Three fundamental equations are necessary to be discretized and solved. In some cases, multiple unclosed terms are determined using additional equations. Continuity equation, conservation of momentum equation, and conservation of energy equation for a generic flow are given, respectively [59].

$$\frac{\partial \rho}{\partial t} + \nabla \cdot (\rho \mathbf{u}) = 0, \tag{3.1}$$

$$\frac{\partial (\rho \mathbf{u})}{\partial t} + \nabla \cdot (\rho \mathbf{u}\mathbf{u}) = -\nabla p + \rho \mathbf{g} + \quad \nabla \cdot (2\mu_{eff}\mathbf{S}(\mathbf{u})) - \nabla \left(\frac{2}{3}\mu_{eff}(\nabla \cdot \mathbf{u}) \right), \tag{3.2}$$

$$\frac{\partial (\rho h)}{\partial t} + \nabla \cdot (\rho \mathbf{u} h) + \frac{\partial (\rho k)}{\partial t} + \nabla \cdot (\rho \mathbf{u} k) - \frac{\partial p}{\partial t} = \nabla \cdot (\alpha_{eff} \nabla h) + \rho \mathbf{u} \cdot \mathbf{g} - \nabla \cdot \dot{q_r'''} + \dot{q'''}. \tag{3.3}$$

In Eqs. 3.1 and 3.2, ρ is the density, u is the velocity field, t is the time, ∇ is nabla-operator defined as $\nabla = \left(\frac{\partial}{\partial x}, \frac{\partial}{\partial y}, \frac{\partial}{\partial z} \right)$, p is the static pressure field, g is the gravitational acceleration, μ_{eff} is the sum of the molecular and turbulent viscosity, and $\mathbf{S}(\mathbf{u})$ is the rate of strain tensor defined as $\mathbf{S}(\mathbf{u}) = \frac{1}{2}\left(\nabla \mathbf{u} + (\nabla \cdot \mathbf{u})^T \right)$. In Eq. 3.3, h is the specific enthalpy, k is the specific kinetic energy, $\dot{q_r'''}$ is the radiative source term, $\dot{q'''}$ is the heat flux from any other source (e.g., combustion), and α_{eff} is the effective thermal diffusivity which is expressed below.

$$\alpha_{eff} = \frac{\rho \nu_t}{Pr_t} + \frac{\mu}{Pr} = \frac{\rho \nu_t}{Pr_t} + \frac{k_f}{c_p}. \tag{3.4}$$

In Eq. 3.4, $\nu_{(t)}$ is the (turbulent) viscosity, $Pr_{(t)}$ is the (turbulent) Prandtl number, k is the thermal conductivity, and c_p is the specific heat.

Close to the interface between the solid and fluid regions, the energy is transported via convection and radiation. Also, a portion of the heat is radiated to the surrounding. Inside the solid, there is only conduction that occurs. The energy conservation equation for the solid is written as

$$\rho_{\mathrm{s}} \frac{\partial T_{\mathrm{s}}}{\partial t} = \nabla \cdot \left(\frac{k_{\mathrm{s}}}{c_{ps}} \nabla T_{\mathrm{s}} \right). \tag{3.5}$$

The methodology and assumptions are explained in the next section.

3.2.2 Simulation Methodology

The CFD model consists of a two-layered specimen under the cone heater surrounded by air. The three solid regions in the computation domain are depicted in Fig. 3.2. The red region is the cone heater with a height of 68 mm, and radii of this truncated cone are 40 mm and 80 mm. A small thickness of 5 mm is assumed for heater elements of the modelled uniform cone. 25 mm below, the specimen is placed. The radius of the cylindrical specimen is 115 mm. The thicknesses of the insulation layer and cement disc are 55 mm, and 7.7 mm, respectively. In Fig 3.2, the air domain is not included for clarity. The surrounding airbox is large enough with the size of 1 m^2 in the x-y plane. All the dimensions used for generating the geometry are presented in Fig. 3.1.

After mesh independence study, the total number of cells selected for the final grid is 331,000. The cartesian grid shows shortcomings in representing the cylindrical specimen in OpenFOAM; it approximates the blocks with small cubes and is not capable of fitting the block into the grid, precisely. Therefore, orthogonal structural mesh in the core region of the specimen and non-orthogonal structural mesh for the rest of the domain are applied. Mesh grading is used so that close to the boundaries between the solid and fluid regions the computational cells become small. The cells are inflated far from the specimen and cone heater with the increase of circumference of the cylindrical specimen in the x-y plane.

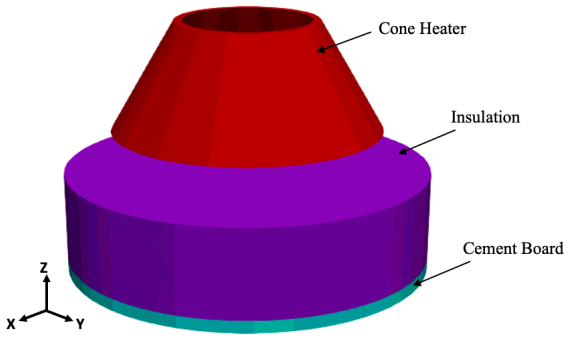

Figure 3.2: The multi-layer specimen under the cone heater in the computational domain. The air domain is removed for clarity.

The minimum and maximum volume sizes are 2.35×10^{-9} m^3 and 7.57×10^{-6} m^3. The thicknesses of the cells in the z-direction are 1.54 mm, 1.67 mm, and 2 mm for the cement disc, the insulation layer, and the cone heater, respectively.

The velocity of the air circulating during the cone calorimeter test is relatively small [71, 72]. Thus, the nature of the fluid flow in the confined box is laminar. Moreover, although there exists convection in the experiment, in this study it is assumed that the air is frozen flow. Therefore, the fluid is stationary, and the velocity terms included in the governing equations become zero for the air region. This simplifying assumption saves the computational cost and improves numerical stability significantly. Although the convective heat transfer is neglected, this is a reasonable assumption because radiation is the most effective heat transfer mechanism in the cone calorimeter tests [10, 73].

Finite volume Discrete Ordinates Method (fvDOM) is selected for modelling the radiation. This is an accurate approach in comparison to other radiation modelling methods such as viewFactor or P1 method. FvDOM solves the radiative transfer equation (RTE) by dividing the participating medium to a specified number of angles. Each ray is emitted from an individual divided angle on each surface. Its intensity is calculated considering the properties participating medium, which is air in this case. A gray constant absorption-emission model with no scattering is selected. A small value of absorptivity and emissivity

of 0.001 is selected for the medium. No soot model is needed since there is no degradation or burning-off during the experiment. The significant portion of heat transfer to the insulation layer is via radiation. Due to conduction, the heat transfers to the underlying layer. No thermal contact resistance is included between the layers.

Pressure Implicit Method for Pressure-Linked Equations or PIMPLE algorithm is selected. Second-order schemes are used for discretizing the diffusion and gradient terms. Temporal derivatives are discretized using a combination of Euler and Crank-Nicolson schemes to have stability and robustness efficiently. The following sections discuss the boundary conditions, the thermophysical properties, and the grid evaluation.

3.2.3 Initial and Boundary Conditions

The computational domain is set to be at the ambient condition, initially. In a study with the same cone calorimeter apparatus, a curve fit for heat flux exposure and cone temperature has been developed [73]. Therefore, for the two incident heat flux values of 25 kW/m^2 and 50 kW/m^2, the temperatures obtained from the profile are 848 K and 1023 K, respectively. These quantities are assigned to the cone heater during the simulation.

3.2.4 Materials Thermophysical Properties

The specimen comprises a layer of ROCKWOOL ® Safe insulation and cement board. Table 3.1 includes the thermophysical properties of the materials in the experiment. The emissivity and specific heat are measured in the University of Waterloo Fire Lab [70], and linear correlations are assumed for the collected data. Emissivity is one of the main parameters here as the primary heat transfer mechanism is radiation. Thermal conductivity is adopted from manufacturer, and a linear profile is assigned to the parameter as a function of temperature [70, 74]. The density for the simulation is assumed to be constant since the mass loss is reported to be less than 2%. The volume remains constant during the exposure to the high incident heat flux values. For the cement board, there are uncertainties left as the exact type is not reported. Therefore, the properties are adopted from an investigation

Parameter	Insulation	cement
Emissivity, ε	$-0.0002\mathrm{T} + 1.0184$	0.54
Thermal conductivity, k (W/mK)	$0.0003\mathrm{T} + 0.0038$	0.227
Specific heat, c_p (J/kgK)	$0.0198\mathrm{T} + 4.6915$	1090
Density, ρ (kg/m^3)	72, constant volume	1150

Table 3.1: Thermophysical properties of the two-layer test case [70, 74, 75, 76]

at the University of Waterloo Fire Lab [73, 75, 76]. This research presents a study on a fire scenario in a compartment composed of different building materials, including cement. Furnace testing on the insulation shows that it undergoes chemical changes that are not taken into account in calculations for emissivity. Shrinkage, binder burn-off and non-uniform mass loss are the phenomena that are suggested to be investigated and modelled in the future CFD models.

3.2.5 Grid Sensitivity Study

A grid sensitivity study is conducted due to two main reasons. The first is that the thermal predictions must be independent of the cell size, meaning that with the increase in grid resolution, the results should not vary drastically. Second, the grid should not be highly resolved due to the high computational costs. During the mesh independence study, the cell numbers are increased to the extent that the variation from the previous case is negligible. The rest of the analysis will be conducted using the final, fine mesh.

Three cases with 107000, 331000, and 556000 cells are considered. Figure 3.3 shows the thermal predictions at the selected locations of T_1, T_2, and T_3 from the beginning of the experiment until reaching a steady state. At the steady-state, the maximum difference to the medium grid is noticed at T_3. The discrepancy between the coarse and fine grids at T_3 is 5.5 %. The discrepancy at T_3 decreases to 0.7 % between the fine and finest grids. The discrepancies at T_1 and T_2 between the fine and finest grids, are 0.23 % and 0.2 % at the steady-state, respectively. In conclusion, the grid with 331,000 cells is sufficient for the current simulations.

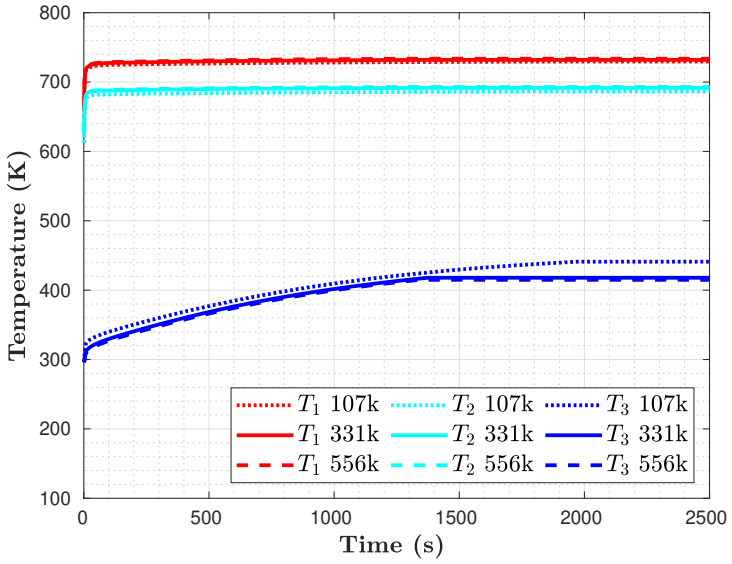

Figure 3.3: Mesh sensitivity analysis on the two-layer specimen.

3.3 Results and Discussion

The case is set up, and the fine mesh is used. Two constant incident heat flux values of 25 kW/m^2 and 50 kW/m^2 are applied to the heater. The temperature predictions (solid line) are compared to experimental data (dotted line) in Figs. 3.4 and 3.5.

The predictions show reasonably good agreement to the experimental data, with some discrepancies exhibiting at the transient section of the profiles on the unexposed side. The temperature at the top surface is predicted well in all cases. The predictions at the central thermocouples are more accurate than the ones closer to the sides.

A closer look at the steady-state values of the temperatures with the heat exposure of 25 kW/m^2 is provided. The temperatures at the exposed surface, T_1 and T_2, are reasonably predicted well. The experimental profiles for these two show that the transient part is very small, and the temperature reaches a steady state quickly. The experimental values for T_1 fluctuates between 733 K to 746 K. T_2 fluctuates between 670 K to 677 K. The modelling results show the steady values of 732 K and 692 K for the T_1 and T_2, respectively.

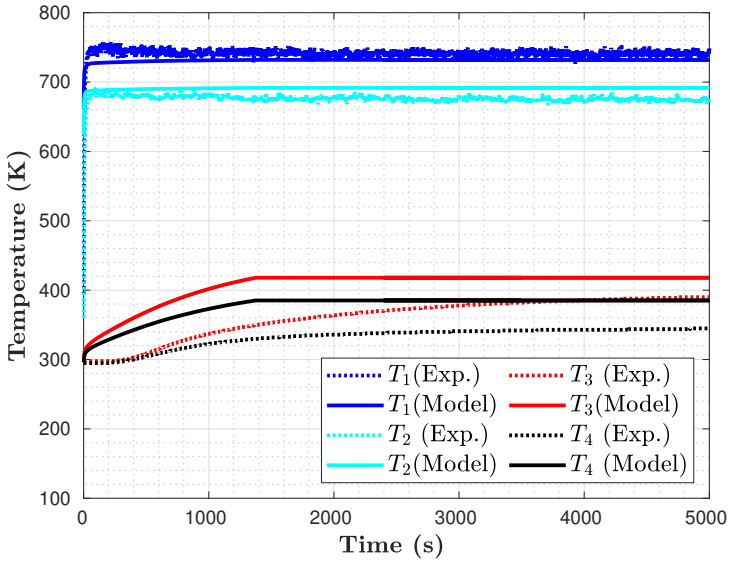

Figure 3.4: Temperature predictions and the experimental data for the constant heat flux exposure of 25 kW/m^2

The model overpredicts the temperatures on the unexposed side of the insulation layer. Both experimental and simulation profiles for T_3 and T_4 display approximately the same trend and slope, although there is a delay in temperature increase during the first 300 seconds, which is not captured. It can be noticed that for both the experimental data and modelling results, the temperature begins to become steady at approximately 1200s. T_3 reaches 391 K, and T_4 reaches 345 K during the experiment. However, the predicted value for T_3 is 418 K, and for T_4, it is 385 K. The same behaviour is noticed for the experiment with the heat exposure of 50 kW/m^2. Table 3.2 shows the percentage differences for the two heat exposures at the latest time.

There are sources of uncertainties in setting up the model resulting in overprediction. The expression for thermal conductivity is the most uncertain thermophysical properties that are used for insulation. Although emissivity and specific heat for the insulation are measured in the experiment, its thermal conductivity may not be accurate. As explained, a linear profile is fitted to data available in the literature for this product, but still, the

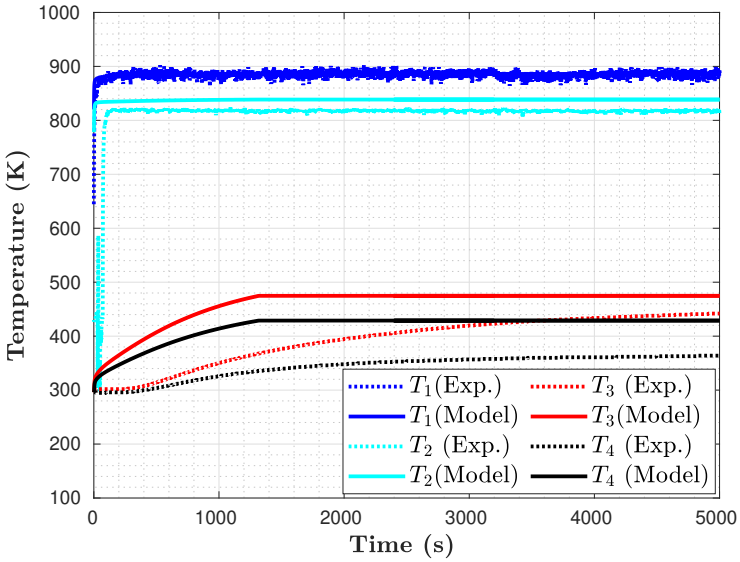

Figure 3.5: Temperature predictions and the experimental data for the constant heat flux exposure of 50 kW/m^2

Exposures	T_1	T_2	T_3	T_4
Exp. 25 kW/m^2	3.8%	1.4%	6.9%	11.6%
Exp. 50 kW/m^2	0.7%	2.7%	8.4%	18.5%

Table 3.2: Percentage difference of the results with the experimental data at the steady state

type of the product is unknown. Moreover, the experimental emissivity modelling does not take into account any chemical reaction the insulation undergoes during the experiment. A lower value for insulation emissivity may diminish the temperature values at the top surface as well as the bottom one. The top surface temperature would decrease as the gray object with lower emissivity absorb less heat from the surroundings. Moreover, it transfers less amount of heat to the bottom layers. Besides, there are fluctuations noticed on the top surface that are sophisticated to model. Lower accuracy is noticed at the unexposed side of the insulation, and the minimum agreement to the model is observed at T_4. There is also a delay in temperature increase during the experiment, which could not be captured. A few reasons are corresponding to this observation. First, there are uncertainties on the cement board type and thermophysical properties, as it is not mentioned in the experimental study. The properties of a cement board at the University of Waterloo Fire Research Lab have been used instead. Since the discrepancies are increased on the unexposed side, it is reasonable to consider the unknown cement type and its properties as the primary uncertainty sources for the CFD model. Second, the thermocouples are welded to the top surface of the cement board, and the insulation layer is comparably light-weighted. Therefore, air gaps exist in between, and the thermal contact is not perfect. The model does not consider the thermal resistance at the interface and the complex heat transfer mechanism that could happen at the boundary. One other reason that may cause the overprediction is neglecting the convection by assuming air as a frozen flow. Although this assumption results in stability and lower computational costs, it contributed to the overpredictions. By considering convection, the air flow can circulate the air and resulting in lower temperature predictions. This is specially important at close to edges (T_2 and T_3) and at the interface of the cement board and insulation (at T_3 and T_4) where the effect of convection for cooling down is more significant.

3.4 Summary

In conclusion, the model predictions agree reasonably with the experimental data. The best predictions are observed at the top thermocouples, and the maximum discrepancies

are noticed at the unexposed side. The overprediction may correspond to various reasons. First, the type and, therefore, the thermophysical properties of the cement are unknown. Second, chemical reactions are not considered in measuring and calculating the insulation emissivity. Third, neglecting convection contributes to the overprediction observed in particular at the interface between the cement disc and insulation. Finally, the complex heat transfer at the interface of the cement board and insulation is not modelled, and no air gap is included in this model.

Chapter 4

Assessment of the Thermal Model for a Three-layer Specimen under a Cone Calorimeter

Chapter 4 extends the application of the CFD model presented in Chapter 3. Investigations are conducted to analyze heat transfer through a three-layer specimen under transient heat exposures in a cone calorimeter test. The experiment details, physics, computational domain, grid, numerical schemes, and thermodynamics properties are presented. Finally, the results are compared to the experimental data, a sensitivity analysis is conducted, and conclusions are made.

4.1 Experimental Details

The experimental study selected for this chapter, describes a three-layer cylindrical specimen which is placed under a cone calorimeter [73]. The specimen comprises a layer of HardieBacker® cement board, three layers of Fiberfrax® Durablanket® S refractory ceramic fibre blanket with a nominal density of 128 kg/m^3, and a layer of hot-rolled A36 steel plate. The diameter of the specimen is 224 mm for all the layers. The large diameter

ensures that there would not be any noticeable deformation for the steel plate, and three-dimensional heat transfer can be captured. The cement board is 10.6 mm thick. This layer would face the minimum thermal effects since it is located under the layers of insulation expected to mitigate heat transfer. On the top of the cement board, three layers of insulation with a thickness of 25.4 mm for a single layer are placed. Finally, the steel plate is 6.20 mm thick. The top surface is entirely polished to make it uniform and remove any oil stains. Then, it is covered with matt black VHT Flameproof® paint. Three thermocouples are welded at the interface of the steel plate and top insulation layer, at the radial distances of 0 mm, 70 mm, and 100 mm. Two other thermocouples are located at equal distances at each layer of the insulation at the centerline. Finally, there is a thermocouple at the interface of the insulation layer and cement board at the centerline. In total, the temperature is measured at six locations to investigate heat transfer in two radial and vertical directions. During the fabrication, the specimen is compressed, so that the final thickness of insulation is 56.0 mm, diminished by 26.5%.

The test case is mounted on the load cell with a 25 mm distance to the bottom of the cone heater. The cone heater is made of tungsten wound heating elements uniformly. The top and bottom diameters of the truncated cone heater are 80 mm and 160 mm, respectively. The height of the cone heater is reported to be 68 mm. Two tests are conducted, in which transient irradiance are applied with two exponentially growing values for incident heat flux, starting from 0 to 25 kW/m^2 (Exposure 1) and 50 kW/m^2 (Exposure 2) at the central line [73]. The schematic of the experiment setup with dimensions is shown in Fig. 4.1.

The experimental study has been selected for the modelling is a modified cone calorimeter test conducted at the University Waterloo Fire Research Facility (UWFRL) [73]. The modifications aimed to address two main subjects. First, unlike the standard tests, which assumes one-dimensional heat transfer, vertically, the experimental study claims that the heat transmitted radially is not negligible. Thus, a wide cylindrical specimen is examined, and the sides are not insulated. Furthermore, generally, the cone calorimeter is preheated before placing the specimen on the load cell. Placing the test case on the load cell must be done quickly and precisely. Besides, any adjustment to the specimen placement would

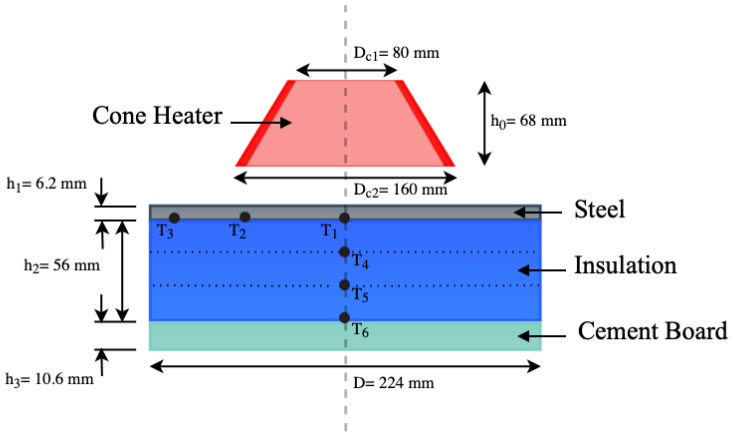

Figure 4.1: Schematic view of the experimental setup including the locations of thermocouple T_1 - T_6

depart the conditions from the standard ones. Therefore, this experiment uses transient incident heat flux [73].

4.2 Computational Details

The computational details are mostly similar to the prescribed ones in Chapter 3. OpenFOAM with solver ChtMultiRegionFoam is used as the main platform to solve the governing equations to predict temperature presented in Section 3.2.1.

Methodology and assumptions are explained in the following sections.

4.2.1 Simulation Methodology

The computational domain constitutes a multi-layer specimen under the cone heater surrounded by air. Figure 4.2 shows the regions, excluding air for clarity. The red region is the cone heater with a height of 68 mm. Radii of this truncated cone are 40 mm and 80 mm. A small thickness of 5 mm is assumed for thickness of the cone heater. 25 mm below,

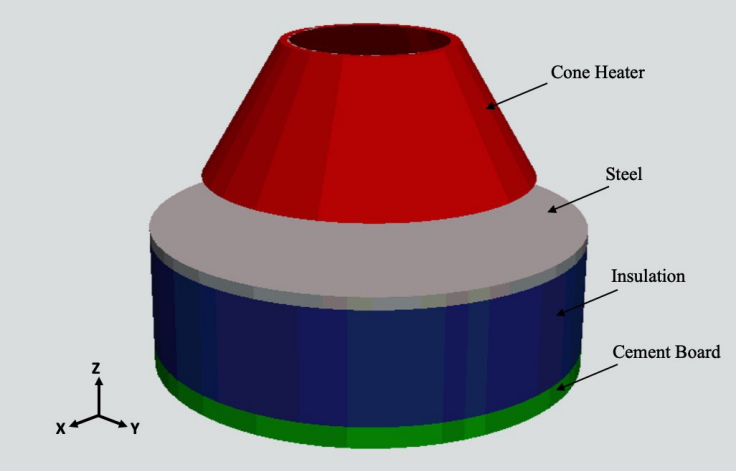

Figure 4.2: The multi-layer specimen under the cone heater in the computational domain. The air domain is removed for clarity.

the specimen is placed. The radius of the cylindrical specimen is 112 mm. The thicknesses of steel, insulation, and cement board are 6.2 mm, 56 mm, and 10.6 mm, respectively. The surrounding airbox is large enough with an area of 1 m^2 in the x-y plane. Figure 4.1 presents the dimensions and locations of thermocouples.

304000 cells are selected for the grid after conducting grid sensitivity analysis. Inflation rates are considered far from the specimen and heater to optimize the computational cost. The minimum and maximum volume sizes are 3.95×10^{-9} m^3 and 7.12×10^{-6} m^3. The lengths of the cells in the z-direction are 2 mm, 2.07 mm, 2.24 mm, and 2.65 mm for the heater, steel, insulation, and cement board.

Frozen flow assumption for air is considered in this model. FvDOM, along with a gray constant absorption-emission model, is used. No thermal contact resistance is included between the layers. This assumption is reasonable since, in this case, there is a heavy-weighted layer on the top of the insulation layer. The compression of the specimen also helps remove air gaps between the layers.

PIMPLE algorithm and second-order schemes for discretizing the diffusion and gradient terms are used. Temporal derivatives are discretized using Euler and Crank-Nicolson

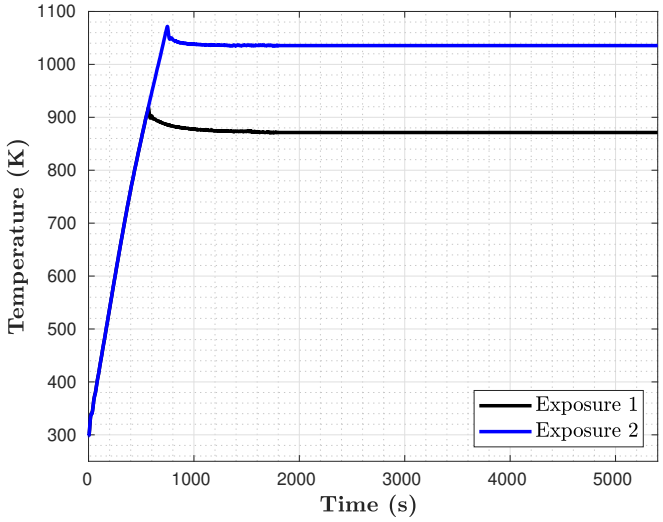

Figure 4.3: The transient cone heater temperature profiles for Exposure 1 and 2

schemes. The difference in the predictions found to be negligible. Thus, the first-order Euler scheme is chosen to reduce computational time for further investigations. The boundary conditions, the thermophysical properties, and the grid evaluation are discussed as follows.

4.2.2 Initial and Boundary Conditions

In the beginning, the whole computational domain is set to the ambient temperature (T=296K) and atmospheric pressure (P=101325 Pa). Figure 4.3 shows two profiles for the temperatures of the cone heater for Exposure 1 (0 to 25 kW/m^2) and Exposure 2 (0 to 50 kW/m^2) [73]. For these two exposures, two transient temperature profiles are applied to all of the heater domain cells, making a uniform heating block at which the temperature increases over time until reaching steady-state temperatures of 871K and 1036K. The cone heater temperature between every two seconds is extrapolated linearly.

4.2.3 Materials Thermophysical Properties

In modelling heat transfer through construction materials, one challenging area is the determination of the thermophysical properties. In this study, the best possible matching properties are selected based on the experiment conditions and the available data in the literature.

The thermophysical properties of the materials used in the multi-layer specimen are presented in Table 4.1. These parameters are taken from different sources. For steel emissivity, various ranges of quantities are available depending on its conditions for roughness, oxidization, and temperature [20, 73]. In this case, the top surface of the steel plate is completely polished and painted, while the unpolished side area is not covered thoroughly in the paint. Moreover, there is a temperature gradient on the surface radially and vertically at the steel plate. The apparent emissivity of the painted steel is estimated at an average experimental surface temperature that the steel is exposed to using an experimental expression for the emissivity of the painted steel plate as follows:

$$\varepsilon\left(T_s\right) = d + \frac{a-d}{1+\left(T_s/c\right)^b} \tag{4.1}$$

Using the equation above, the emissivity is calculated at the surface temperature of T_s in Kelvin. The coefficients of a, b, c, and d are 0.9339, 2.902, 342.2, and 0.9916, respectively. The coefficient of determination for the developed expression is 0.9928 [73]. Between the range of the minimum and maximum temperatures during two exposures, T_s=300 K to T_s=880 K, the calculated emissivity alters from 0.957 to 0.988. By increasing the temperature, the rate of changes of the quantity reduces, and gradually the apparent emissivity gets close to one. The rest of the thermophysical properties of steel are taken from a study in which heat transfer through a typical black painted steel plate attached to an insulation layer in a cone calorimeter test was investigated [77].

The properties of the insulation are adopted from various sources [78, 33, 79]. It is worth mentioning that for this experiment, the insulation is compressed by approximately 26.5%. Therefore, the density differs from the nominal one. Additionally, it generates uncertainties

for the values of the thermal conductivity and specific heat. The thermophysical properties of the cement board are mostly taken from studies conducted at the University of Waterloo Fire Research Lab [75, 76, 73].

Parameter	Steel	Insulation	Cement
Emissivity, ε	0.97	0.85	0.54
Thermal conductivity, k (W/mK)	42	0.05	0.227
Specific heat, c_p (J/kgK)	$486.522 + 161.044(T/1000) + 418.014(T/1000)^2$	1130	1090
Density, ρ (kg/m^3)	$7850/(1 + 0.004[(T - 273.15)/1000]^6)$	94.18	1150

Table 4.1: Thermophysical properties of the materials of the three-layer specimen

4.2.4 Grid Sensitivity Study

Grids with the sizes of 134000, 304000, and 476000 cells are used to check mesh sensitivity. The temperature profiles at three selected points are shown in Fig. 4.4. The maximum discrepancy is noticed at one of the thermocouples inside the insulation layers, T_5, between the coarse and fine grids. The percentage difference compared to the fine grid is 2.2%. There is no noticeable difference between the fine and finest grids; therefore, the mesh with 304,000 cells is selected for further investigations.

4.3 Results and Analysis

After setting up the case, two exponentially growing heat exposures are applied to the cone heater. The results of the simulations for Exposure 1 using constant and temperature-dependent properties for steel are presented. Figures 4.5 and 4.7 show the temperature profiles for T_1, T_2, and T_3 located at the unexposed surface of the steel plate. Furthermore, Figs. 4.6 and 4.8 show the predictions for T_4, T_5, and T_6 across the insulation. The dotted lines are the experimental profiles, and the solid lines are the simulations results. The profiles show the importance of considering accurate temperature-dependent thermophysical properties, rather than constant ones, particularly at the transient parts of the

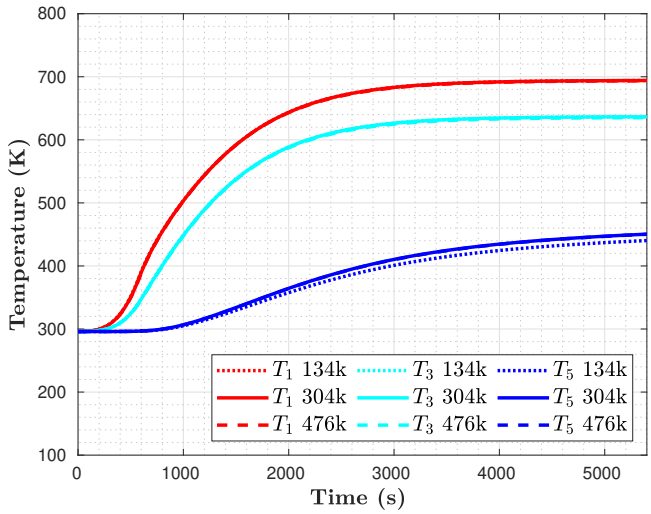

Figure 4.4: Mesh sensitivity analysis for the simulation of the three-layer specimen

profiles. The improvement in predicting the transient evaluation results in more accuracy for the steady-state temperatures. This effect is mostly noticed at T_6. Therefore, it can be concluded that temperature-dependent properties improve the predictions. Figures 4.9 and 4.10 present the simulation results for the experiment with Exposure 2, which are the temperature profiles at the unexposed side of the steel plate and through the insulation layers.

The results of the CFD model show good agreement to the experimental data, in particular at the end of the experiments. The simulation results follow the same trend as the experimental values in these six profiles. While the experiment (Exposure 1) gives the temperatures of 669 K, 657 K, 633 K, 569 K, 457 K, and 328 K for T1 - T_6 at the end of the experiment, the simulated quantities are 694 K, 666 K, 636.5 K, 563 K, 450 K, and 349 K, respectively. The experimental and simulation data match reasonably. The experimental values for Exposure 2 are 871 K, 811 K, 759 K, 714 K, 558 K, and 353 K for the thermocouple locations mentioned above. The simulation results are 845 K, 797 K, 745 K, 664 K, 510 K, and 370 K. Table 4.2 presents the percentage differences for Exposures 1 and 2 using temperature-dependent properties for both cases at the final time steps. Compared

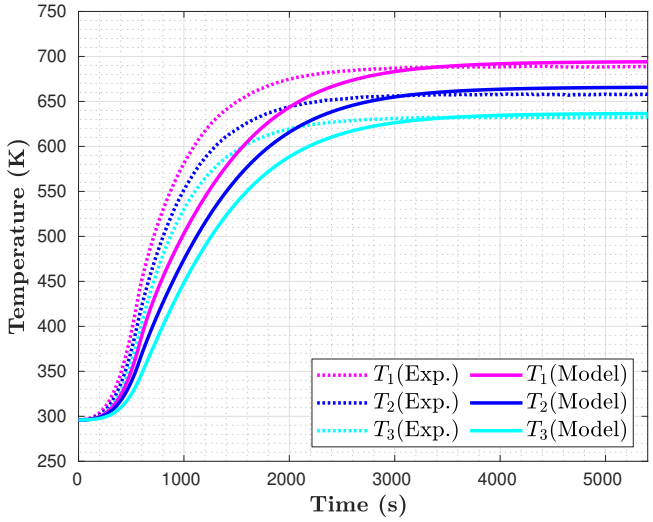

Figure 4.5: Temperature profiles at the exposed side of the steel plate using constant thermophysical properties, Exposure 1

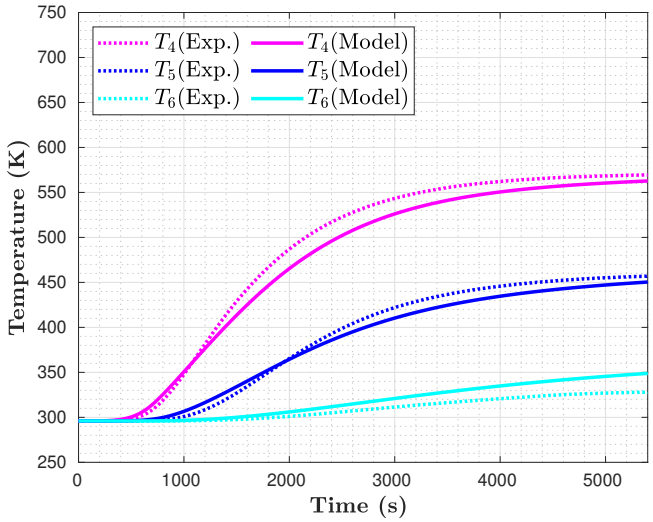

Figure 4.6: Temperature profiles at the unexposed side of the steel plate using constant thermophysical properties, Exposure 1

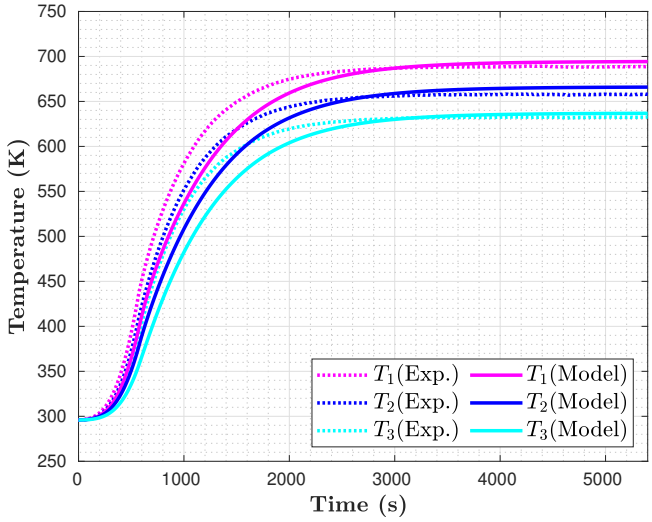

Figure 4.7: Temperature profiles at the exposed side of the steel plate using temperature-dependant thermophysical properties, Exposure 1

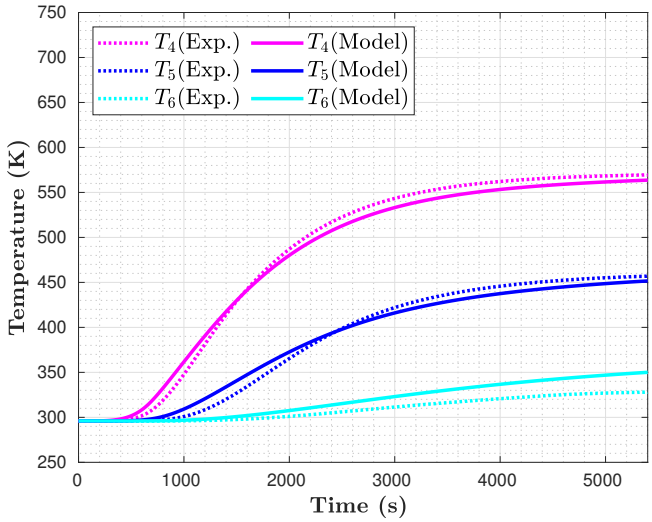

Figure 4.8: Temperature profiles at the unexposed side of the steel plate using temperature-dependant thermophysical properties, Exposure 1

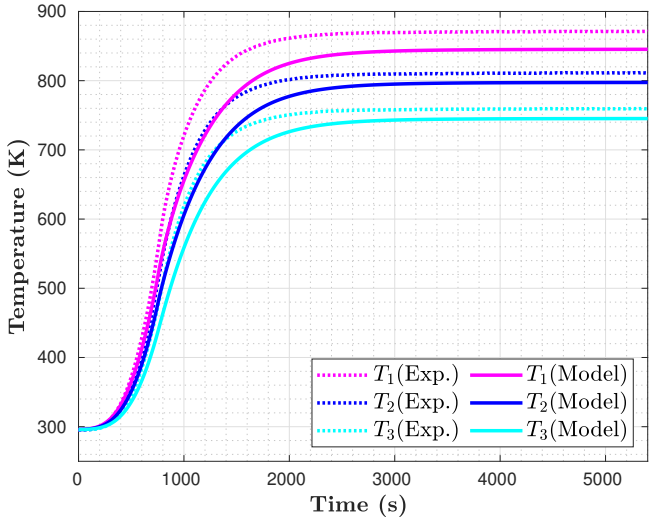

Figure 4.9: Temperature profiles at the exposed side of the steel plate, Exposure 2

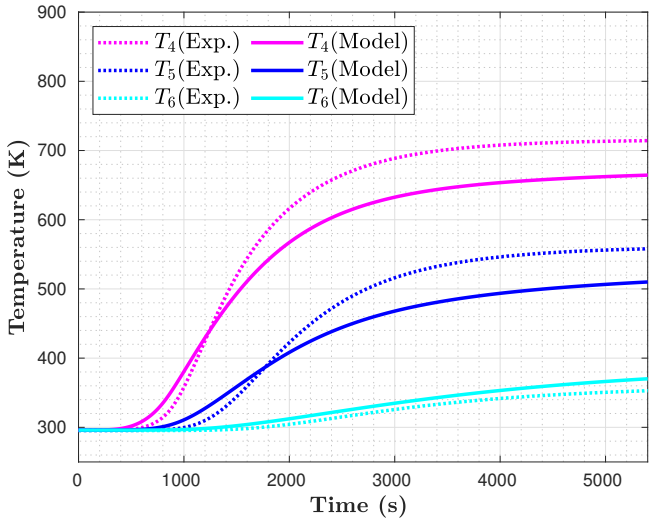

Figure 4.10: Temperature profiles at the unexposed side of the steel plate, Exposure 2

to Exposure 2, the simulated quantities for Exposure 1 are more accurate. Furthermore, the highest discrepancies are observed at the thermocouples through the insulation layers.

The maximum percentage difference is 9% at T_5 for Exposure 2. For Exposure 1, at T_1 - T_3, and T_6 small underpredictions are noticed. The maximum discrepancy is at T_6 with an underprediction of 6%. For Exposure 2, at all of the thermocouple locations except T_6, an overprediction can be noticed.

Exposures	T_1	T_2	T_3	T_4	T_5	T_6
Exposure 1	0.8%	1.2%	0.6%	1.2%	1.5%	6.3%
Exposure 2	2.9%	1.2%	1.2%	6.7%	8.6%	4.9%

Table 4.2: Percentage difference between the simulations results and the experimental data for the multi-layer specimen at the steady state

Three factors contribute to the discrepancies. First of all, there are uncertainties on the type of steel and its properties. The properties adopted from an experiment in which the type of the steel plate is not specified. Also, the emissivity that is assumed to be constant for all the polished and non-polished surfaces and all temperatures. Although the top surface is painted in black in order to make the emissivity constant close to one, the small side surfaces may have impact in the heat transfer calculations. Second, constant properties are used for insulation due to limited information. It is reasonable that the maximum discrepancies are observed through insulation layers. Using temperature-dependent properties for the specific type of insulation can improve the predictions significantly. Furthermore, the thermophysical properties of insulation are selected at an uncompressed state, while in the experiment, the material is compressed by 26.5%. The compression process removes the air within the pores in insulation. Therefore, the assumption of no thermal contact is more accurate in this case, and predictions agree with the experimental values at T_6. However, this generates uncertainies and the real properties change compared to the values in data sheets. With the air removal, the insulation transfers more heat and the thermal conductivity is increased. This results in higher temperature predictions across the insulation. Finally, adding convection to the simulation can help the modelled specimen to cool down more by circulated air and results in less overpredictions in particular close to the edges such as at T_6.

In conclusion, the CFD model is capable of well-predicting the temperature of a spec-

imen in the cone calorimeter test. the discrepancies are believed to be mostly caused by uncertainties of the thermophysical properties of the material, in particular at the elevated temperatures.

4.3.1 Sensitivity Analysis

The conductivity, density, specific heat, and emissivity of the steel plate are modified in order to investigate the sensitivity of the simulation results to these parameters. The specimen is exposed to the exponentially growing heat flux of 25 kW/m^2. Each parameter is changed for 20% of its initial value, except for the higher quantity for emissivity, which is one at its maximum.

Respectively, the thermal predictions are displayed in Figs. 4.11 - 4.14 for T_1 to T_3 and T_4 to T_6. Each plot includes three lines for each temperature measurement assigned to three values of a specific parameter. The results for the main case are shown with solid lines. Table 4.3 shows the differences (in percentage) for the temperature predictions at the latest time steps compared to the main simulation.

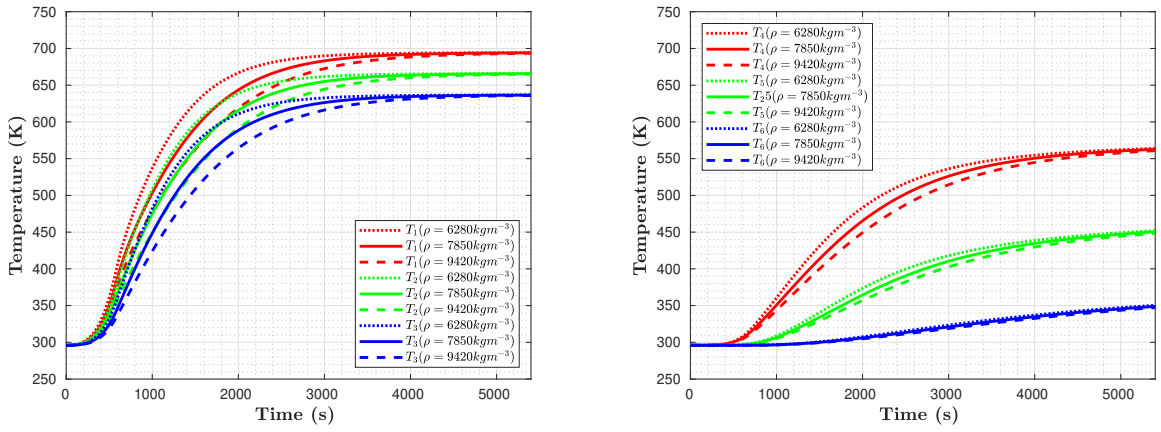

(a) (b)

Figure 4.11: Temperature profiles (a) under the steel plate and (b) through the insulation using three values for the steel density

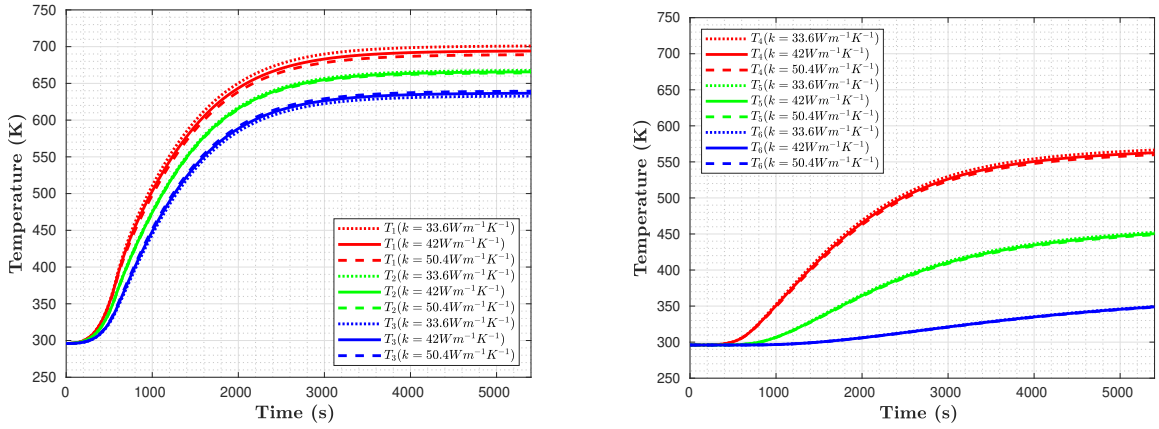

(a) (b)

Figure 4.12: Temperature profiles (a) under the steel plate and (b) through the insulation using three values for the steel conductivity

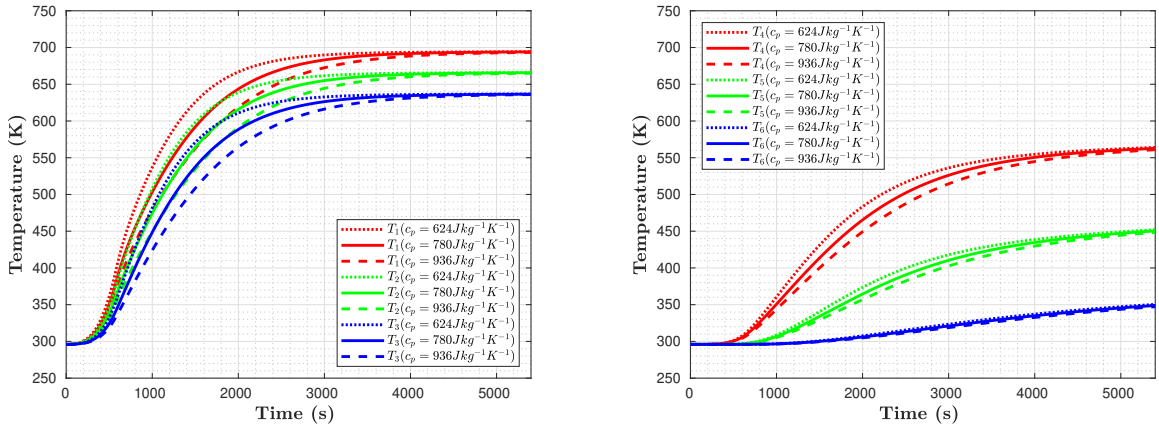

(a) (b)

Figure 4.13: Temperature profiles (a) under the steel plate and (b) through the insulation using three values for the steel specific heat

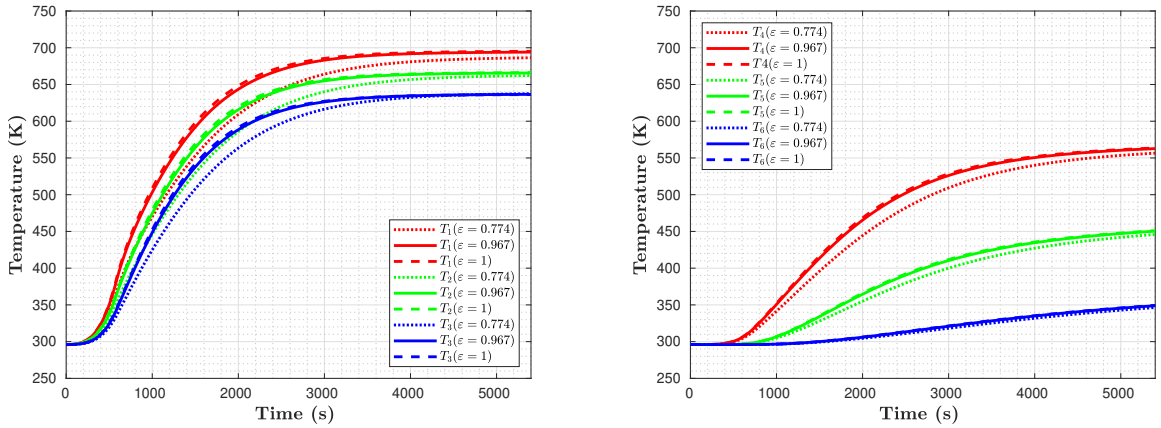

(a) (b)

Figure 4.14: Temperature profiles (a) under the steel plate and (b) through the insulation using three values for the steel emissivity

As seen in Table 4.3, the results show the most significant sensitivity to changing the emissivity and then the conductivity of the steel at the latest time steps. Furthermore, the contributions of changing the density and specific heat are the same, and similar behaviour is noticed. In the radial direction, T_1 at the center line is the most affected location. Additionally, in the vertical direction, it can be noticed that the changes in the parameter of the top layer (steel) parameters affect the thermal predictions in the insulation layer as the amount of transmitted heat to the layer varies. Among the thermocouples in the insulation layer, T_4 is the most affected one in the most of the cases. Unlike all the parameters, decreasing the steel emissivity results in lower temperature predictions. This is due to the fact that a smaller emissivity causes the gray object to absorb less heat from the surroundings. A closer look at the transient part of the predictions shows that the most considerable changes in the trends of the profiles are noticed for the emissivity, presented in Fig 4.14. The next significant impacts are generated by changing the density and specific heat, while they do not greatly affect the final thermal predictions. Finally, changing the conductivity does not change the trend of profiles noticeably.

The study shows that steel emissivity is the most crucial property in the simulation

Parameters	T_1	T_2	T_3	T_4	T_5	T_6
ρ(+20%)	-0.09	-0.10	-0.10	-0.33	-0.47	-0.47
ρ (-20%)	0.04	0.04	0.04	0.22	0.37	0.43
k(+20%)	-0.73	-0.21	0.43	-0.51	-0.32	-0.12
k (-20%)	0.98	0.29	-0.61	0.68	0.43	0.17
c_p(+20%)	-0.09	-0.10	-0.10	-0.33	-0.47	-0.47
c_p(-20%)	0.04	0.04	0.04	0.22	0.37	0.43
$\varepsilon = 1$	0.16	0.07	-0.05	0.15	0.13	0.09
ε(-20%)	-1.1	-0.54	0.16	-1.1	-1.0	-0.72

Table 4.3: Sensitivity of the results to the properties of the steel at the latest time step in percentage

and for providing accuracy. The condition of the steel (e.g., colour, polishing) can change the emissivity and should be taken into account. Additionally, there are different types of steel plates, and the properties may vary based on the type. Since the properties of the steel plate are taken from different studies, good improvements in the simulation result are possible using the exact properties of the type. Among all, determination of the emissivity and conductivity are the most important ones.

4.4 Summary

In this chapter, a description of extending the usage of the CFD model to a non-degrading multi-layer specimen is presented. Two values of transient heat flux are applied to the specimen during the tests. The results show that the model can predict thermal measurements in the cone calorimeter tests. The model predictions agree with the experimental data. At the elevated temperatures of Exposure 2, underprediction is observed. The discrepancies can be correlated to the fact that there are some uncertainties sources in the thermophysical properties of the materials and neglected air circulation. Furthermore, a sensitivity study is conducted to measure the relative impact of the thermophysical proper-

ties of steel. It is concluded that the results are mostly affected by changing the emissivity and conductivity. The predictions of the trends can also improve by using more accurate values for the specific heat and density.

Chapter 5

Full-scale Compartment Fire Model

The previous chapters investigated heat transfer in small-scale tests as the first steps toward developing a model for predicting heat transfer in fire scenarios. This chapter studies the large-scale modelling of an experimental fire test. Besides the fundamental physics and developments in small-scale CFD models, in modelling a compartment fire, turbulent fluid flow of hot gases circulating in the room increases the rate of heat transfer. These gases are heated up by combustion of the fuel, increasing the room temperature, and, consequently, making radiation a critical part of the model. In modelling a fire scenario, all heat transfer mechanisms play significant roles in heat transfer to the walls and surroundings.

This chapter outlines the development of a fire model for an experimental study conducted at the University of Waterloo Fire Research Lab, using OpenFOAM. The experimental and numerical details, including the boundary conditions, formulations, grid, and properties of the materials, are presented. Also, sub-models for radiation, combustion, and turbulent flow considered for fire modelling are explained. Next, the results are compared to the experimental data. Finally, conclusions are made, and a summary is given.

5.1 Experimental Details

The experimental study is conducted to provide extensive temperature measurements in a fire compartment [10]. It aims to provide information on the behaviour of two kinds of non-degrading steel and degrading wood-framing walls in a fire. In total, 17 tests are conducted with different fuel sizes, fuel configurations, ventilation conditions, and types of walls. Fire test apparatus is a modified shipping container with interior dimensions of 3.5 m $\times$ 2.3 m $\times$ 2.3 m. A doorway is located on one of the short sides of the compartment with the dimension of 0.8 m $\times$ 2.0 m. On the other side, there is a removable steel wall in place that separates the fire room from the transitional room. The apparatus is instrumented with thermocouples that measure the temperature at four corners of the fire room and on three racks at eight heights on the steel wall. The height of the sensors ranges from 0.3 m to 2.1 m.

Figure 5.1: Softwood crib bundle used in the experiment; taken from [10]

The selected test is conducted at the ambient condition of T=23.3°C and P=97.38 kPa. The interior walls and ceiling of the container are thoroughly insulated with panels of ceramic fibre insulation and cement boards to mitigate heat transfer to the exterior frame. Fiberfrax Durablanket S® refractory ceramic fibre blanket with a nominal density of 128 kg/m^3 is used as a suitable material for elevated temperatures to protect the structure from fire. For the steel wall, 18 gauge sheet steel is used. After polishing and removing oil

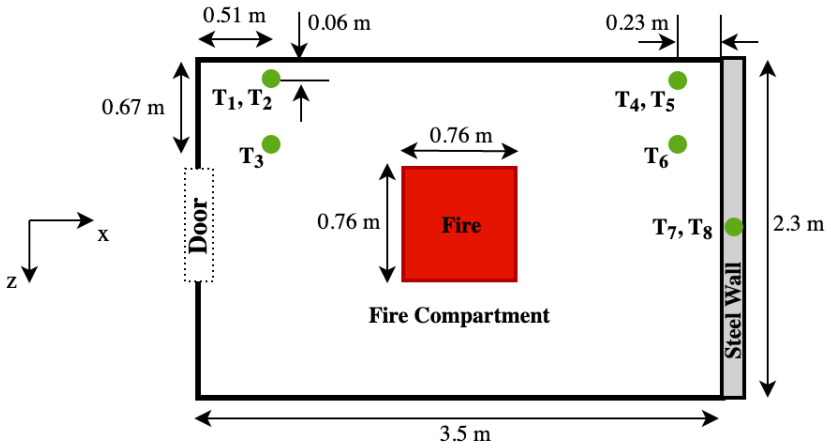

Figure 5.2: View of the fire compartment with dimensions and the locations of thermocouples

strains, it is covered with matte black VHT Flameproof® paint on both sides. The door is partially open with a brick (6.3 cm gap) to provide airflow. The fuel consists of a softwood crib bundle and small pieces of red oak with an approximate mass of 8 kg. The fuel size is 0.76 m × 0.76 m, placed at the center of the fire compartment. Its size is almost half of the standard wood crib and is pictured in Fig. 5.1.

Thermocouples are selected in a way to show temperatures at low, moderate, and high heights. They are located at two corners of the fire room and on the steel wall. T_1 and T_4 are at an equal height of h=0.3 m, T_2 and T_5 are at a height of h=0.9 m, and T_3 and T_6 are at a height of h=2.2 m. Finally, T_7 and T_8 measure the temperature at heights of h=1.1 m and h=2.1 m, respectively. The fire compartment, dimensions, and instrumentation are displayed in Fig. 5.2.

5.2 Computational Details

OpenFoam and a solver named FireFOAM are used for the simulation. Capabilities of FireFOAM for various fire scenarios are investigated in different studies [61, 68, 69, 80]. The general governing equations needed to be solved for modelling a compartment fire are conservation of mass, conservation of momentum, conservation of energy and species transport equation. Sub-models for turbulence, heat transfer, and combustion provide additional equations presented in this section.

5.2.1 Governing Equations

Spatially filtered, Favre-averaged or density-weighted averaged sets of the governing equations are used by FireFOAM [15]. In fire scenarios, significant variations in density occur during combustion due to great deviations from the ambient temperature at the initial stage of the experiment. The temperature reaches up to 1000K in some cases. Therefore, Favre-averaged governing equations are appropriate to use [81]. Continuity, conservation of momentum, energy transport, and species transport equations are given in Eqs. 5.1 - 5.4, respectively [15].

$$\frac{\partial \bar{\rho}}{\partial t} + \frac{\partial \bar{\rho}\tilde{u}_j}{\partial x_j} = 0, \tag{5.1}$$

$$\frac{\partial \bar{\rho}\tilde{u}_i}{\partial t} + \frac{\partial \bar{\rho}\tilde{u}_i\tilde{u}_j}{\partial x_j} = -\frac{\partial \bar{p}}{\partial x_j} + \frac{\partial}{\partial x_j}\left(\bar{\rho}\left(\nu + \nu_t\right)\left(\frac{\partial \tilde{u}_i}{\partial x_j} + \frac{\partial \tilde{u}_j}{\partial x_i} - \frac{2}{3}\frac{\partial \tilde{u}_k}{\partial x_k}\delta_{ij}\right)\right) + \bar{\rho}g_i, \tag{5.2}$$

$$\frac{\partial \bar{\rho}\tilde{h}}{\partial t} + \frac{\partial \bar{\rho}\tilde{u}_j\tilde{h}}{\partial x_j} = \frac{D\bar{p}}{Dt} + \frac{\partial}{\partial x_j}\left(\bar{\rho}\left(D_h + \frac{\nu_t}{Pr_t}\right)\frac{\partial \tilde{h}}{\partial x_j}\right) - \nabla \cdot \dot{q}_r''' + \dot{q}''', \tag{5.3}$$

$$\frac{\partial \tilde{\rho}\tilde{Y}_k}{\partial t} + \frac{\partial \bar{\rho}\tilde{u}_j\tilde{Y}_k}{\partial x_j} = \frac{\partial}{\partial x_j}\left(\bar{\rho}\left(D_Y + \frac{\nu_t}{Sc_t}\right)\frac{\partial \tilde{Y}_k}{\partial x_j}\right) + \overline{\dot{\omega}}_{Y_k}. \tag{5.4}$$

In the equations above, filtered quantities are represented with $(\tilde{.})$, ρ is the density, u is the velocity field, t is the time, x_j is the Cartesian coordinate, p is the hydrostatic pressure field, and $\nu_{(t)}$ is the (turbulent) kinematic viscosity. In Eq. 5.2, δ_{ij} is the Kronecker delta which is 0, except at $i = j$ at which it is equal to 1, and g_i is the gravitational acceleration in ith direction. In Eq. 5.3, h is the total specific enthalpy, D_h is the thermal laminar diffusion coefficient, Pr_t is the turbulent Prandtl number, ∇ is nabla-operator defined as $\nabla = \left(\frac{\partial}{\partial x}, \frac{\partial}{\partial y}, \frac{\partial}{\partial z}\right)$, $\dot{q_r'''}$ is the radiative source term, $\dot{q'''}$ is the additional source term considers the chemical reactions. In Eq. 5.4, Y_k is the mass fraction of species k, D_Y is the species laminar diffusion number, Sc_t is the turbulent Schmidt number, $\dot{\omega}_{Y_k}$ is the chemical reaction rate.

5.2.2 Turbulence Modelling

Typically, for turbulent flows in fire scenarios, LES is a suitable approach for turbulence modelling. Conservation of momentum equation in FireFOAM is altered as follows [15]:

$$\frac{\partial \bar{\rho}\tilde{u}_i}{\partial t} + \frac{\partial \bar{\rho}\tilde{u}_i\tilde{u}_j}{\partial x_j} = -\frac{\partial \bar{\rho}}{\partial x_i} + \frac{\partial \bar{\sigma}_{ij}}{\partial x_j} - \frac{\partial \tau_{ij}^{sgs}}{\partial x_j}. \tag{5.5}$$

In Eq. 5.5, p is the hydrostatic pressure, σ_{ij} is the viscous stress tensor, and τ_{ij}^{sgs} is the subgrid scale (SGS) stress tensor. Two later parameters are given by

$$\tau_{ij}^{sgs} = \bar{\rho}\left(\widetilde{u_i u_j} - \tilde{u}_i\tilde{u}_j\right), \tag{5.6}$$

$$\bar{\sigma}_{ij} = \mu\left(2\tilde{S}_{ij} - \frac{2}{3}\tilde{S}_{kk}\delta_{ij}\right), \tag{5.7}$$

where μ is the dynamic viscosity, and S_{ij} is the rate of strain tensor described as

$$\tilde{S}_{ij} = \frac{1}{2}\left(\frac{\partial \tilde{u}_i}{\partial x_j} + \frac{\partial \tilde{u}_j}{\partial x_i}\right). \tag{5.8}$$

In LES, large scale eddies are explicitly calculated, whereas the small scale motions are modelled. The proper cutoff wavenumber $\kappa_c = \pi/\Delta$ with the grid width Δ lies at

the inertial sub-range and splits the energy spectrum into two sections mentioned above [82]. The subgrid-scale stress tensor (τ_{ij}^{sgs}) must be modelled to close the conservation of momentum equation (Eq. 5.5). Among the available methods for SGS closure, the k-equation eddy viscosity model is selected. In this approach, a model for subgrid turbulent viscosity is employed which is expressed by

$$\nu_t = C_k \sqrt{k_{sgs}} \Delta, \tag{5.9}$$

where $C_k = 0.05$, Δ is the grid size, and k_{sgs} is the SGS turbulent kinetic energy determined by $k_{sgs} = \tau_{ii}^{sgs}/2$. The transport equation for the SGS turbulent kinetic energy is shown in Eq 5.10.

$$\frac{\partial \bar{\rho} k_{sgs}}{\partial t} + \frac{\partial \bar{\rho} k_{sgs} \tilde{u}_j}{\partial x_i} = \bar{\rho} \left(\tau_{ij}^{sgs} \frac{\partial \tilde{u}_i}{\partial x_j} \right) - \bar{\rho} C_\epsilon \frac{k_{sgs}^{3/2}}{\Delta} + \frac{\partial}{\partial x_i} \left(\bar{\rho} \left(\nu + \frac{\nu_t}{\sigma_k} \right) \frac{\partial k_{sgs}}{\partial x_i} \right), \tag{5.10}$$

where $C_\epsilon = 1.048$, $\sigma_k = 1$ by default. In Eq. 5.10, on the right hand side, the production, dissipation, and diffusion terms are presented, respectively. The SGS stress tensor (τ_{ij}^{sgs}) is correlated to the SGS turbulent viscosity and SGS turbulent kinetic energy expressed as

$$\tau_{ij}^{sgs} = \frac{2}{3} k_{sgs} \delta_{ij} - 2\nu_t \overline{S_{ij}}. \tag{5.11}$$

where δ_{ij} is the Kronecker delta [83].

5.2.3 Combustion

The Damköhler number is a parameter to determine applicable combustion model defined as

$$D_a = \tau_t / \tau_c, \tag{5.12}$$

where τ_t is the turbulent (mixing) time scale, and τ_c is the chemical time scale. In a mixing controlled scenario where τ_c is relatively smaller to τ_t or $Da >> 1$, an infinitely fast chemistry assumption is made, meaning that reaction rates only depend on the rate of

turbulent mixing [84]. A fire scenario is one of the cases where this assumption is applicable. The Eddy dissipation concept (EDC) approach is typically used in these cases where the flow is highly turbulent. Simplicity and a wide range of applications make EDC a common model in industry and research communities [68]. A filter equation for the reaction rate of fuel is employed for the closure of Eq. 5.4 given by

$$\overline{\dot{w}}_{Y_k} = \frac{\overline{\rho}}{\min\left(\tau_t/C_{EDC}, \tau_{\text{diff}}/C_d\right)} \min\left(\tilde{Y}_F, \tilde{Y}_{O_2}/r_s\right), \tag{5.13}$$

where ρ is the density, τ_t is the turbulent mixing time, τ_{diff} is the diffusion time scale, C_{EDC} and C_d are the model coefficients, Y_F and Y_{O_2} are the fuel and oxygen mass fractions, and r_s is the stoichiometric oxygen to fuel ratio [15].

Chemistry

Wood is a complex material when it comes to chemistry and pyrolysis. It comprises cellulose, hemicellulose, and lignin. The relative portions of these components vary from one type of wood to another, but typically, almost half of wood is made of cellulose [2, 85]. Cellulose is a string shaped, high-weighted molecular can be found only in nature. In contrast to cellulose, hemicellulose is a branch-shaped molecule with a lower molecular weight. Lignin is the most complex structure which brings strength to the combination and binds the other constituents together. Thermal degradation and pyrolysis of wood components occur simultaneously and go through different paths producing volatile gases, char and ash. The decomposition starts from 200°C for hemicellulose and continues to 500°C for lignin [86]. From 200°C to close to 450°C, wood discolours and a half portion of lignin replaced by char [2]. Moreover, volatile gases and smoke circulate into the wood slabs through the cracks, which may lead to secondary reactions between these gaseous products and char residues [85].

For modelling of wood chip combustion, Rajika and Narayana considered wood as a type of biomass which generates volatile gaseous products (e.g., CO, CH_4, H_2) , and char during combustion [87]. Pyrolysis of biomass with partial oxidation at elevated temperatures may produce methanol during intermediate reactions in the presence of CO, CH_4, CO_2, H_2, and

H_2O [88, 89]. Assuming a one-step reaction of methanol reduces the complexity of wood pyrolysis, which has been used previously [73]. This assumption might be appropriate as methanol is generated during the intermediate reactions of biomass, but may oversimplify the case as it removes the other reactions such as char combustion and soot formation. The reaction is given by

$$CH_3OH + 1.5O_2 + 5.76N_2 \rightarrow CO_2 + 2H_2O + 5.76N_2 \tag{5.14}$$

5.2.4 Heat Transfer

At the selected thermocouple locations, OpenFOAM utility functions are employed to collect the thermal predictions. Eq. 5.15 is the energy conservation equation used to consider the effect of heat transfer to each thermocouple bead as follow [15]

$$\rho_{TC} C_{p,TC} V_{TC} \frac{dT_{TC}}{dt} = \epsilon_{TC} \left(G - \sigma T_{TC}^4 \right) A_{TC} + h \left(T_g - T_{TC} \right) A_{TC}, \tag{5.15}$$

where TC represents the thermocouple, ρ is the density, C_p is the specific heat, V is the volume, T is the temperature, ϵ is the emissivity, G is the average irradiance received, is the Stefan-Boltzmann constant, A is the surface area, h is the coefficient of convective heat transfer, and T_g is the local gas temperature.

Close and into the walls, all heat transfer modes are modelled. In addition to the doorway, the heat leaves the compartment via conduction through the walls. The ceiling and three sides of the compartment are equipped with boards of insulation and cement, while on one side of the compartment, the steel wall is placed, which can easily transfer heat. Through the walls, one-dimensional conduction is assumed to save computational cost.

Finite Volume Discrete Ordinates Method (FvDOM) is employed; constant gray absorption-emission model and non-scattering medium are assumed. No soot or pyrolysis model is needed for the combustion of methanol.

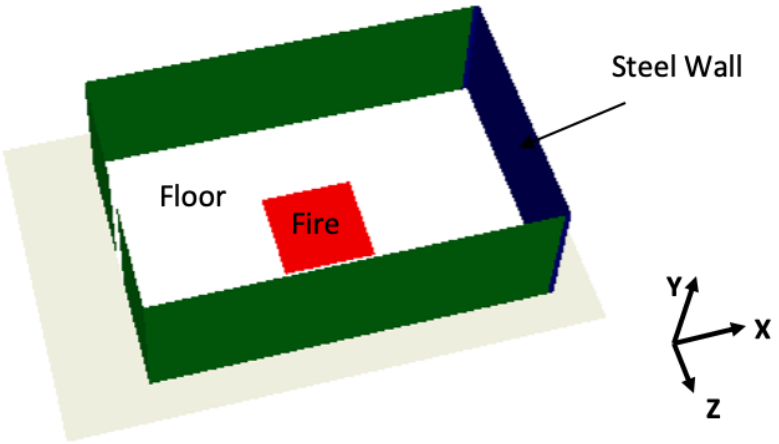

Figure 5.3: Cross-sectional view of the computational domain

5.2.5 Simulation Methodology

The computational domain consists of the fire compartment modelled in a larger region to maintain the airflow to the surroundings through the doorway. Figure 5.3 shows a cross-sectional view of the fire compartment. On the right side, the steel wall shown in blue is located; the fire shown with a red square is centred in the room, and the other walls are shown in green colour. The fire room with the interior dimensions of 3.5 m $\times$ 2.3 m $\times$ 2.3 m, and the larger cubic area has a size of 4.6 m $\times$ 3.2 m $\times$ 3.0 m.

After the mesh sensitivity study for grids with 353000 cells, 580000 cells, and 730000 cells, a final mesh with 580,000 cells is selected. The grid is uniform with a cell size of 4.7 cm with the refinement in the fire region where the cell size is 2.3 cm. Another parameter for optimizing the grid in fire modelling is the characteristic fire diameter, which is calculated using Eq. 5.16 [90]

$$D^* = \left(\frac{\dot{Q}}{\rho_\infty T_\infty c_p \sqrt{g}} \right)^{2/5}, \tag{5.16}$$

where D^* is the characteristic fire diameter, $\dot{Q}$ is the heat release rate, g is the gravity acceleration, ρ_∞ is the air density at ambient temperature, T_∞ is the ambient temperature, and c_p is the specific heat. It is recommended that $4 < D^*/\max(\delta x, \delta y, \delta z) < 16$ for sufficient resolution [91] . In this criterion, δx, δy, and δz are the cell dimensions in the x, y, and z directions in fire region. The accuracy increases for the higher ratios. The ratio of $D^*/\max(\delta x, \delta y, \delta z)$ is approximately 14 for the current study.

FvDOM solves the radiative transfer equation (RTE) by dividing the medium into numbers of solid angles. Generally, in fire scenarios, 48 solid angles are adequate, considering accuracy and computational cost [92, 73]. In this study, the total numbers of 64 rays are selected for the FvDOM for more accuracy. An experimental coefficient (χ_r), which determines the ratio of heat in radiation to the total amount of heat, is assumed to be $\chi_r = 0.364$ for softwood crib [2].

The case is set up to the ambient conditions for the initial conditions. For the extended air box, the velocity at the patch boundary is set to act as an inlet/outlet based upon the calculated pressure. For most of the properties of the compartment walls and ceiling, a zero gradient boundary condition is employed. No-slip boundary condition for the velocity at the walls and ceiling is used. Also, one-dimensional conduction for the fire compartment walls and ceiling is employed. The fire is modelled as an inlet with a specified mass flow rate. The mass loss rate (MLR) is approximated using the softwood heat release rate experimentally measured at the UWFRL and heat of combustion for methanol (ΔH_c) [10, 2, 73]. Using $\Delta H_c = 725$ kJ/mol in $\dot{Q} = \chi \dot{m}_f{}'' A_f \Delta H_c$, the MLR is determined at each time step; interpolation is used when required. The maximum calculated HRR in the fire simulation is 124.3 kW which is almost half of the maximum experimental value of 250 kW. Since the softwood crib in the selected experimental study is weighted half of the standard one which is 16 kg, it is rational that the maximum heat release rate is half the standard one. Therefore, this is a proper approach to follow.

Pressure Implicit Method for Pressure-Linked Equations (PIMPLE) algorithm is selected. The temporal terms are discretized using the first-order Euler scheme. The diffusion and gradient terms are mostly discretized using a second-order accurate Gauss linear scheme. A maximum Courant number of 0.7, along with the initial time step of 0.001s,

Parameter	Steel	Insulation	Cement
Thermal conductivity, k (W/mK)	42	0.05	0.227
Specific heat, c_p (J/kgK)	487	1130	1090
Density, ρ (kg/m^3)	7850	128	1150

Table 5.1: Thermophysical properties of the wall construction materials [10, 33, 76, 77, 78, 79]

provides convergence and stability during the simulation.

5.2.6 Materials Thermophysical Properties

The materials used in constructing the fire compartment are similar to the ones in Chapter 4. Table 5.1 represents the thermophysical properties of the steel wall, Fiberfrax Durablanket S® refractory ceramic fibre blanket, and cement board adopted from various sources [10, 33, 76, 77, 78, 79]. The insulated walls are equipped with panels of 12.7 mm thick cement and 25.4 mm insulation. Therefore, the effective thermophysical properties are determined using appropriate thicknesses to use in the modelling. At the elevated temperatures, the specific heat values for the gases are calculated using the polynomial coefficients from NASA tables [93].

5.3 Results and Analysis

Figures 5.4- 5.6 represent the simulation temperature results (solid lines) compared to the experimental data (dotted lines). T_1, T_2, and T_3 are the thermocouples located near the steel wall at the heights of $h_1 = 0.3$ m, $h_2 = 0.9$ m, and $h_3 = 2.2$ m. The equivalent thermocouples are selected on the other side of the room close to the doorway at the same heights. Thermocouples T_7 and T_8 are selected at heights of 1.1 m and 2.2 m.

As seen in Fig. 5.4, faster changes in temperature are predicted in both growth and decay phases. The maximum predicted temperatures for T_1, T_2, and T_3 are 371 K, 521

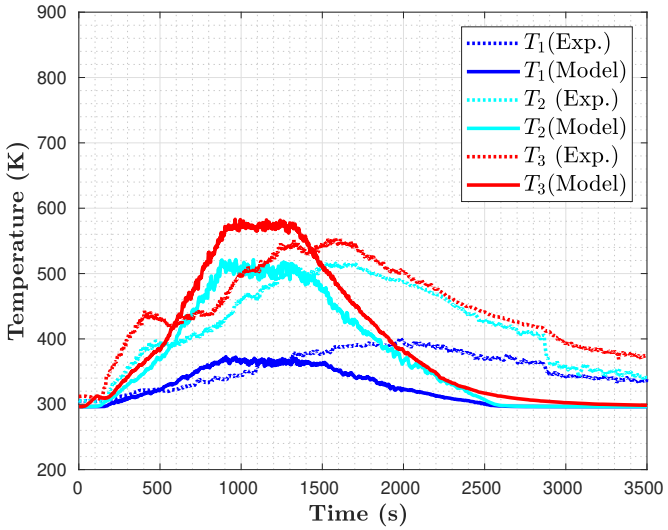

Figure 5.4: Temperature profiles for T_1, T_2, and T_3

K, and 581 K, whereas the maximum experimental values are 401 K, 515 K, and 554 K, respectively. The results show good agreement in the growth phase of the fire test, especially for the first 500s. The same behaviour is noticed at T_4 - T_6. As shown in Fig. 5.5, the model is capable of predicting the temperature better close to ventilation. The model captured the experimental data trend for the growth phase, particularly for the first 1000s at T_4, but the discrepancies got noticeable at the decay phase. The maximum simulation results for T_4, T_5, and T_6 are 340 K, 521 K, and 564 K, while the maximum experimental results are 390 K, 513 K, and 533 K. Fig. 5.6 shows underprediction for T_7 and T_8. The maximum values of T_7 and T_8 for the simulation are 550 K and 555 K, while the measurements are 449 K and 456 K. T_7 profile follows the same pattern as T_8 profile in both the prediction and experiment.

One main possible reason for the discrepancies is the simplifying assumption of the methanol combustion instead of wood. An accurate wood pyrolysis model, volatile gaseous product, and char combustion can make the results more accurate. The char residues may have prolonged burning, while they are generated during wood pyrolysis. This may result in a higher temperature during the decay phase for all the thermocouple locations. An-

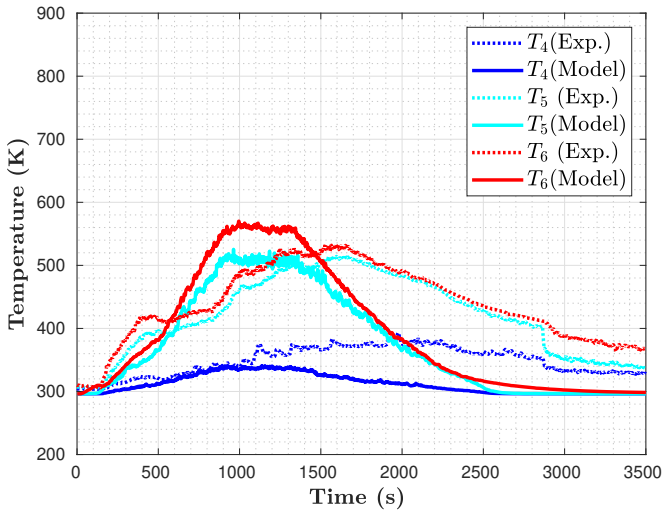

Figure 5.5: Temperature profiles for T_4, T_5, and T_6

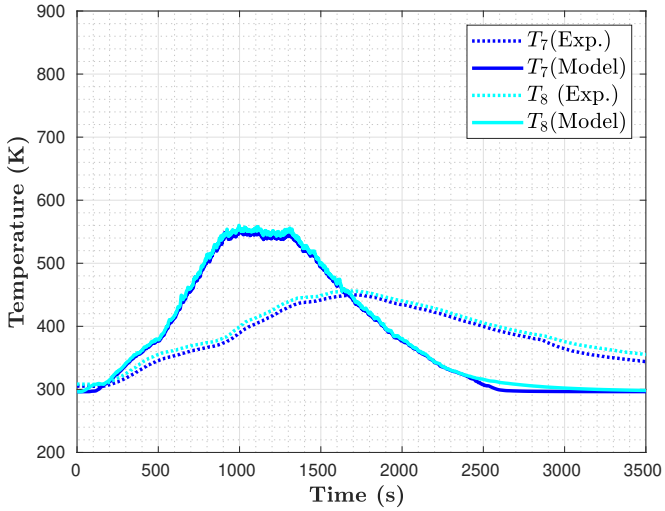

Figure 5.6: Temperature profiles for T_7 and T_8

other room for improvement is adding the transitional room to the computational domain. Although removing it saves the computational costs, considering the room in the simulation may increase the temperature at T_7 and T_8 at the decay phase. Due to the high conductivity of steel, the steel wall transmits heat at a high rate. In the case of existing transitional room, heat transfer occurring at the steel wall may result in more accurate thermal predictions as a portion of air does not leave the computational domain at the boundaries of the extended box on one side. Finally, the results may improve by adding a three-dimensional conduction mechanism through the walls to accurately model heat loss.

5.4 Summary

In this chapter, a fire model developed to predict temperature measurements at the selected thermocouples at different heights in a fire compartment. The fire compartment is insulated on three walls and ceiling, while it is separated from a transitional room with a steel wall. A softwood crib is ignited at the centre of the room during the test. The model can capture the trend in the growth phase, particularly for the first 1000s near the doorway, but discrepancies become noticeable during the decay phase. This can be due to three main reasons. First, a simplified methanol pool is used instead of softwood cribs. Therefore, no pyrolysis or soot model is considered, which provides a less complicated case. Char and volatile combustion as secondary reactions may provide a prolonged burning model, which increases the temperature at the decay phase. Second, the insulated transitional room is removed to save computational cost. Finally, three-dimensional conduction through the walls may improve the predictions. Overall, this fire model can be used as a first step toward a more complex one that can predict material behaviours in compartment fires.

Chapter 6

Conclusions

This work numerically investigated small-scale and large-scale experiments to develop CFD models for predicting the behaviour of construction building materials in fire scenarios.

Chapters 3 and 4 focused on assessing the heat transfer calculations for specimens during cone calorimeter tests. In Chapter 3, the thermal performance of a two-layer specimen consists of ROCKWOOL® Safe insulation and cement disc exposed to constant heat flux is modelled, using OpenFOAM. The temperature predictions were compared to the measurements, which showed a reasonably good agreement, particularly at the top thermocouples. Discrepancies occurred at the maximum at the unexposed non-central thermocouple, which may correspond to the fact that cement board type and properties are not entirely known. Also, considering air circulation in the experimental setup and the air gap at the interface of insulation and cement disc could increase the accuracy. Chapter 4 assessed the heat transfer model and extended it to model three-layer specimen under transient heat exposure in a cone calorimeter. The specimen was made of steel, Fiberfrax® Durablanket® S refractory ceramic fibre blanket, and HardieBacker® cement disc. The simulation results matched the measurements, and the small discrepancies are believed to correspond to uncertainties in the thermophysical properties of the materials. A sensitivity study on the properties of steel showed that the results are most sensitive to steel emissivity. Therefore, it is a crucial property that needs to be accurately determined and modelled.

Chapter 5 described modelling a large-scale fire compartment. In the experiment, a softwood crib at the centre of the fire room was burning. The fire compartment was separated from a transitional room with a steel wall. The compartment was insulated with panels of insulation and cement boards. The temperature was measured at different locations in the fire compartment and on the steel wall. The model of a fire compartment was developed using FireFOAM. LES was used for modelling turbulence; the EDC model was used for combustion, and the FvDOM model was employed for radiation. The results showed good agreement in the growth phase, especially at the first 500s and near the doorway at the compartment, but underprediction was noticed at the decay phase. The development of this model is the first step toward an advanced model for predicting the thermal performance of building construction materials and fire compartments. For the future work, enhancements can be made for modelling wood pyrolysis, considering the transitional room in the computational domain, and 3D conduction through the walls.

References

[1] S. Turns, *An introduction to combustion, concepts and applications*. New York, NY: Mc Graw Hill, third ed., 2012.

[2] D. Drysdale, *An introduction to fire dynamics*. Chichester, West Sussex, England: John Wiley Sons, third ed., 2011.

[3] N. DaÈic, *Fire investigation*. Boca Raton, Florida: CRC Press LLC, 2004.

[4] S. Porter, *The great fire of London*. The History Press, 2011.

[5] F. Armstrong, *A city in the making*. Dundurn Press, 1988.

[6] P. Morris, *Embattled shadows: a history of Canadian cinema, 1895-1939*. McGill-Queen's Press, 1992.

[7] A. Withey, "Bushfire season starts early across northern Australia due to ongoing hot, dry conditions," *ABC News*, 2019.

[8] B. Ries, V. Rocha, R. Picheta, E. McKirdy, J. Yeung, G. Mezzofiore, and P. Murphy, "Fire at Notre Dame Cathedral," *CNN*, 2019.

[9] L. Audouin, L. Rigollet, H. Pretrel, W. LeSaux, , and M. Rowekamp, "OECD PRISME project: fires in confined and ventilated nuclear-type multi-compartments - overview and main experimental results," *Fire Safety Journal*, vol. 62, pp. 80–101, 2013.

[10] M. Didomizio, *Experimental study of thermal degradation of fire resisting compartment partitions in fires*. PhD thesis, University of Waterloo, 2017.

[11] D. Sahua, S. Jainb, and A. Gupta, "Experimental and numerical simulation studies on diesel pool fire," *Fire and Material Journal*, vol. 40, no. 10, pp. 1016–1035, 2016.

[12] D. Sahua, S. Jainb, A. Gupta, and Shashia, "Experimental study on methanol pool fires under low ventilated compartment," *Procedia Earth and Planetary Science*, vol. 11, pp. 507–515, 2015.

[13] M. Janssen, *Calorimetry, 905-951*. New York, NY: Springer New York, 2016.

[14] M. Lui, Y. He, and V. Beck, "Application of field model and two-zone model to fashover fires in a full-scale multi-room single level building," *Fire Safety Journal*, vol. 29, pp. 1–25, 1997.

[15] "OpenFOAM." http://www.openfoam.com/. Accessed: 2018-09-01.

[16] FM. Global, "FireFOAM-dev," 2018.

[17] W. Chen, J. Ye, Y. Bai, and X. Zhao, "Thermal and mechanical modeling of load-bearing cold-formed steel wall systems in fire," *Journal of Structural Engineering*, vol. 140(8), 2014.

[18] S. Sinha, A. Jhalani, M. Ravi, and A. Ray, "Modelling of pyrolysis in wood: a review," *SESI Journal*, vol. 10(1), pp. 41–62, 2000.

[19] W. Park, *Study of pyrolysis of charring materials and its application to fire safety and biomass utilization*. PhD thesis, University of Michigan, 2008.

[20] F. Incropera, D. Dewitt, T. Bergman, and A. Lavine, *Fundamentals of heat and mass transfer*. John Wiley and Sons, sixth ed., 2011.

[21] J. Quintiere, *Principles of fire behavior*. NY, US: Delmar Cengage Learning, 1998.

[22] V. Babrauskas and R. Peacock, "Heat release rate: the single most important variable in fire hazard," *Fire Safety Journal*, vol. 18, pp. 255–272, 1992.

[23] S. Pope, *Turbulent flows*. Cambridge University Press, 2000.

[24] Y. Zhiyin, "Large-eddy simulation: past, present and the future," *Chinese Journal of Aeronautics*, vol. 28, pp. 11–24, 2015.

[25] J. Smagorinsky, "General circulation experiments with the primitive equations in the basic experiment," *Monthly Weather Reviews*, vol. 91(3), pp. 99–164, 1963.

[26] B. Karlsson and J. Quintiere, *Enclosure fire dynamics*. Boca Raton, Florida: CRC Press LLC, 1999.

[27] G. Thomas, "Modelling thermal performance of gypsum plasterboard-lined light timber frame walls using SAFIR and TASEF," *Fire and Material Journal*, vol. 34, pp. 385–406, 2010.

[28] V. Kodur and T. Harmathy, *Properties of building materials. In SFPE Handbook of Fire Protection Engineering*. Quincy, MA: National Fire Protection Association, fourth ed., 2008.

[29] L. Richardson, "Thoughts and observations on fire-endurance tests of wood-frame assemblies protected by gypsum board," *Fire and Material Journal*, vol. 25, pp. 223–230, 2001.

[30] H. Takeda and J. Mehaffey, "WALL2D: a model for predicting heat transfer through wood-stud walls exposed to fire," *Fire and Material Journal*, vol. 22, pp. 133–140, 1998.

[31] S. Bhatia, *Advanced renewable energy systems*. Woodhead Publishing India Pvt., 2014.

[32] P. Clancy, "Advances in modelling heat transfer through wood framed walls in fire," *Fire and Material Journal*, vol. 25, pp. 241–254, 2001.

[33] A. Papadopoulos, "State of the art in thermal insulation materials and aims for future developments," *Energy and Building Journal*, vol. 367(1), pages=, 2005.

[34] H. Takeda, "A model to predict fire resistance of non-load bearing wood-stud walls," *Fire and Material Journal*, vol. 27, pp. 19–39, 2003.

[35] D. Lázaro, E. Puente, M. Lázaro, P. Lázaro, and J. Peña, "Thermal modelling of gypsum plasterboard assemblies exposed to standard fire tests," *Fire and Material Journal*, vol. 40, pp. 568–585, 2016.

[36] Q. Yu and H. Brouwers, "Thermal properties and microstructure of gypsum board and its dehydration products: a theoretical and experimental investigation," *Fire and Material Journal*, vol. 36, pp. 575–589, 2012.

[37] A. Korte and H. Brouwers, "Calculation of thermal conductivity of gypsum plasterboards at ambient and elevated temperature," *Fire and Material Journal*, vol. 34, pp. 55–75, 2010.

[38] S. Craft, B. Isgor, J. Mehaffey, and G. Hadjisophocleous, "Modeling heat and mass transfer in wood-frame floor assemblies exposed to fire," *Fire Safety Science*, vol. 9, pp. 1303–1314, 2008.

[39] G. Hadjisophocleous, N. Benichou, and A. Tamim, "Literature review of performance-based fire codes and design environment," *Journal of Fire Protection Engineering*, vol. 9, pp. 12–40, 1998.

[40] M. Puchovsky, "NFPA's perspectives on performance-based codes and standards," *Fire Technology*, vol. 32, p. 323–332, 1996.

[41] B. Meacham and R. Custer, "Performance-based fire safety engineering: an introduction of basic concepts," *Journal of Fire Protection Engineering*, vol. 7(2), pp. 35–54, 1995.

[42] A. Alvarez, B. J. M. N. A. Dembsey, and J. R. Thomas, "Twenty years of performance-based fire protection design: challenges faced and a look ahead," *Journal of Fire Protection Engineering*, vol. 23(4), pp. 249–276, 2013.

[43] *National Building Code of Canada 2015 (NBC)*. Ottawa, ON, 2015.

[44] *ASTM E119-16a. Standard Test Methods for Fire Tests of Building Construction and Materials*. West Conshohocken, PA, 2016.

[45] *CAN/ULC-S114-05. Standard Method of Test for Determination of Non- combustibility in Building Materials.* Ottawa, ON, 2005.

[46] *ASTM E1354-17. Standard Test Method for Heat and Visible Smoke Release Rates for Materials and Products Using an Oxygen Consumption Calorimeter.* West Conshohocken, PA, 2016.

[47] *ASTM E967-08. Standard Test Method for Temperature Calibration of Differential Scanning Calorimeters and Differential Thermal Analyzers.* West Conshohocken, PA, 2016.

[48] *ASTM E968-02. Standard Practice for Heat Flow Calibration of Differential Scanning Calorimeters.* West Conshohocken, PA, 2016.

[49] *ASTM 603-17. Standard Guide for Room Fire Experiments.* West Conshohocken, PA, 2016.

[50] *ASTM E2257. Standard Test Method for Room Fire Test of Wall and Ceiling Materials and Assemblies.* West Conshohocken, PA, 2016.

[51] P. V. Hees, "Validation and verification of fire models for fire safety engineering," *Procedia Engineer*, vol. 62, pp. 154–168, 2013.

[52] H. E. Mitler and J. Rockett, "A users' guide to first comprehensive single-room fire model," tech. rep., Gaithersburg, MD, 1987.

[53] H. Mitler, "The physical basis for the Harvard Computer Fire Code," home fire project technical report no. 34, Harvard University, 1978.

[54] H. Mitler and H. Emmons, "Documentation for computer fire code V, The 5th Harvard Computer Fire Code," tech. rep., Harvard University, 1981.

[55] J. Quintiere, "Fundamentals of enclosure fire 'zone' models," *Journal of Fire Protection Engineering*, vol. 1, pp. 99–119, 1989.

[56] V. Babrauskas, "Fire modeling tools for FSE: Are they good enough?," *Journal of Fire Protection Engineering*, vol. 8, pp. 87–93, 1995.

[57] R. Peacock, W. Jones, P. Reneke, and G. Forney, "CFAST - consolidated model of fire growth and smoke transport (version 6) users' guide," NIST Special Publication 1041, 2005.

[58] J. Cadorin, "On the application field of Ozone V2," rapport interne no ms/2002-003, Département de Mécanique des matériaux Structures, Universite de Liege, 2002.

[59] H. Versteeg and W. Malalasekera, *An introduction to computational fluid dynamic: the finite volume method*. Pearson Education Limited, second ed., 2007.

[60] P. Roache, *Verification and validation in computational science and engineering*. Hermosa, 1998.

[61] A. Brown, M. Bruns, M. Gollner, J. Hewson, G. Maragkos, A. Marshall, R. McDermott, B. Merci, T. Rogaume, S. Stoliaro, J. Torero, A. Trouvé, Y. Wang, , and E. Weckman, "Proceedings of the first workshop organized by the IAFSS working group on Measurement and Computation of Fire Phenomena (MaCFP)," *Fire Safety Journal*, vol. 101, pp. 1–17, 2018.

[62] "ANSYS Fluent 19.0," 2018.

[63] "ANSYS CFX 19.0," 2018.

[64] "COMSOL Multiphysics 5.5," 2019.

[65] "ISIS. Developed the Institut de Radioprotection et de Súrete Nucleaire." https://gforge.irsn.fr/gf/project/isis. Accessed: 2018-02-01.

[66] "FDS. Developed by the National Institute of Standards and Technology in collaboration with the VTT Technical Research Centre of Finland." https://pages.nist.gov/fds-smv. Accessed: 2018-02-01.

[67] "SIERRA/Fuego. Developed by Sandia National Laboratories," 2017.

[68] D. Le, J. Labahn, T. Beji, C. Devaud, E. Weckman, and A. Bounagui, "Assessment of the capabilities of FireFOAM to model large-scale fires in a well-confined and mechanically ventilated multi-compartment structure," *Journal of Fire Science*, vol. 36(1), pp. 3–29, 2018.

[69] G. Maragkos, P. Rauwoens, and B. Merci, "Application of FDS and FireFOAM in large eddy simulations of a turbulent buoyant helium plume," *Combustion Science and Technology Journal*, vol. 33(2), pp. 2473–2480, 2012.

[70] N. Nagy, "Determination of thermal properties of mineral wool insulation materials for use in full-scale fire modelling," Master's thesis, University of Waterloo, 2020.

[71] J. Staggs, "Convection heat transfer in the cone calorimeter," *Fire Safety Journal*, vol. 44(4), pp. 469–474, 2009.

[72] J. Staggs, "A reappraisal of convection heat transfer in the cone calorimeter," *Fire Safety Journal*, vol. 46(3), pp. 125–131, 2011.

[73] D. Wilson, "Numerical simulations of small-scale and full-scale fire experiments," Master's thesis, University of Waterloo, 2018.

[74] N. Benichou, M. Sultan, C. MacCallum, and J. Hum, "Thermal properties of wood, gypsum and insulation at elevated temperatures," *NRC Publication Archive*, 2001.

[75] "Emissivity Coefficients of Materials." www.engineeringtoolbox.com/emissivity-coefficients-d_447.html. Accessed: 2018-12-01.

[76] A. Klinck, *An Experimental Investigation of the Fire Characteristics of the University of Waterloo Burn House Structure*. PhD thesis, University of Waterloo, 2006.

[77] J. Zhang and M. Delichatsios, "determination of the convective heat transfer coefficient in three-dimensional inverse heat conduction problems," *Fire Safety Journal*, vol. 44(5), pp. 681–690, 2009.

[78] "Fiberfrax Durablanket S: Product Information Sheet." https://www.unifrax.com/product/fiberfrax-durablanket-s/. Accessed: 2018-12-01.

[79] M. Redmond and A. Mastropietro, "Thermophysical and optical properties of materials considered for use on the LDSD test vehicle," (Vellevue, WA, Texas University), 2015.

[80] A. Trouve and Y. Wang, "Large eddy simulation of compartment fires," *International Journal of Computational Fluid Dynamics*, vol. 24(10), pp. 449–466, 2010.

[81] C. Chen, J. Riley, and P. McMurty, "A study of favre averaging in turbulent flows with chemical reaction," *Combustion and Flames Journal*, vol. 87(3-4), pp. 257–277, 1991.

[82] B. Chaouat, "The state of the art of hybrid RANS/LES modeling for the simulation of turbulent flows," *Flow, Turbulence and Combustion*, vol. 99, p. 279–327, 2017.

[83] S. Menon, P. Yeung, and W. Kim, "Effect of subgrid models on the computed interscale energy transfer in isotropic turbulence," *Computers and Fluid*, vol. 25(2), pp. 165–180, 1996.

[84] B. F. Magnussen and B. H. Hjertager, "On mathematical models of turbulent combustion with special emphasis on soot formation and combustion," *Symposium (International) on Combustion*, vol. 16(1), pp. 719–729, 1976.

[85] A. Roberts, "Problems associated with the theoritical analysis of the burning of wood," *Fire Technology*, vol. 13(1), pp. 893–903, 1971.

[86] A. Bartlett, R. Hadden, and L. Bisby, "A review of factors affecting the burning behaviour of wood for application to tall timber construction," *Fire Technology*, vol. 55, pp. 1–49, 2019.

[87] J. Rajika and M. Narayana, "Modelling and simulation of wood chip combustion in a hot air generator system," *SpringerPlus*, vol. 5(1), 2016.

[88] M. Balat, "Experimental study on pyrolysis of black alder wood," *Energy Exploration and Exploitation*, vol. 26(4), pp. 209–220, 2008.

[89] Y. Zhang, J. Xiao, and L. Shen, "Simulation of methanol production from biomass gasification in interconnected fluidized beds," *Industrial Engineering Chemistry Research*, vol. 48(11), pp. 5351–5359, 2009.

[90] A. Bounagui, N. Bénichou, C. McCartney, and A. Kashef, "Optimizing the grid size used in cfd simulation to evaluate fire safety in houses," *NRC Publication Archive*, pp. 1–8, 2003.

[91] B. Husted, Y. Li, C. Huang, J. Anderson, R. Svensson, H. Ingason, M. Runefors, and J. Wahlqvist, "Verification, validation and evaluation of firefoam as a tool for performance design," Brandforsk report, Lund University, 2017.

[92] P. Chatterjee, Y. Wang, K. Meredith, and S. Dorofeev, "Application of a subgrid soot-radiation model in the numerical simulation of a heptane pool fire," *Proceeding to Combustion Institute*, vol. 35(3), pp. 2573–2580, 2015.

[93] B. McBride, S. Gordon, and M. Reno, "Coefficients for calculating thermodynamic and transport properties of individual species.," NASA technical memorandum 4513, 1993.